Physical and Compositional Studies of Comet 81P/Wild 2 at Multiple Apparitions

Tony L. Farnham

Department of Astronomy
University of Maryland
College Park, MD 20742

and

David G. Schleicher

Lowell Observatory
1400 W. Mars Hill Road
Flagstaff, AZ 86001
email: dgs@lowell.edu

Accepted for publication in Icarus

Abstract

We present analyses and results from both narrowband photometry and CCD imaging of Comet 81P/Wild 2 from multiple apparitions, obtained in support of the Stardust mission. These data include photometric measurements from 12 days before the encounter and imaging from 3 days after. Using narrowband photometry from the different apparitions, we analyzed the dust and gas production rates as a function of heliocentric distance, finding a substantial seasonal effect where the production of OH, NH and dust peaks 11–12 weeks before perihelion. The CN, C_2 and C_3 production show no such asymmetry, suggesting that there may be heterogeneities among different sources on the nucleus. The water production peaked at a level of approximately 1.1×10^{28} molecules s^{-1} in 1997. A comparison of the relative abundances of minor gas species places Wild 2 in the "depleted" category in the A'Hearn et al. (1995) taxonomic classifications. Continuum measurements at multiple wavelengths indicate that the comet has a low dust-to-gas ratio, with moderately reddened dust. In our images we see a dust tail, an anti-tail and two well-defined jets. The primary jet, which persists for several months and is roughly aligned with the spin axis, has a source latitude $>+75°$, while the secondary jet is located on the opposite hemisphere between $-37°$ and $-62°$. We used the apparent position angle of the primary jet to determine the pole orientation, α=281$\pm$5°, δ=+13$\pm$7°, and surmise that the nucleus is likely in a state of simple rotation. The primary source is continuously illuminated when Wild 2 is inbound and turns away from the Sun at about the time that the comet reaches perihelion, explaining the seasonal effects in the production rates. We measured lightcurves on several observing runs but saw no significant modulation, so no constraints can be set on the rotation rate. Images at different wavelengths show that the jets have the same colors as the dust in other regions in the coma and tail, indicating that the grain properties are similar throughout the coma. Radial profiles of the coma were measured in various directions on a number of different observing runs, and we discuss the findings from these measurements. Finally, we compare our results with other published data and attempt to predict future times at which observations should be obtained to help constrain additional properties.

Keywords: Wild 2, comets, photometry, composition, rotational dynamics, Coma

1 Introduction

Following a close encounter (<0.01 AU) with Jupiter in 1974, comet 81P/Wild 2 was discovered in early January 1978. Before the Jupiter encounter the comet had a perihelion distance (q) of 5.0 AU (E. Bowell, private communication, 2004), so the 1978 apparition, where q=1.49 AU, may represent Wild 2's first passage inside the orbit of Mars. If so, it is likely to be less altered and less thermally evolved than most Jupiter family comets (JFC). A subsequent perturbation by Jupiter in 1986 shifted q out to 1.58 AU.

Narrowband photometric observations of Wild 2 were obtained during the 1978 (A'Hearn and Millis 1980) and 1983/84 apparitions, and a summary of results from these two data sets was presented by Osip et al. (1992) as part of a study of JFCs that were considered to be viable spacecraft targets. After comet Wild 2 was selected as the target for the Stardust mission, we took advantage of the 1997 apparition to conduct a dual-instrument observing campaign to obtain as much information about the comet as possible in support of the mission. At the request of the Stardust team, we also made a special effort to obtain photometric measurements of Wild 2 in 2003 to confirm whether it was behaving as predicted around the time of the encounter. Unfortunately, the 2003/04 apparition was an extremely poor one, with the comet and Earth on opposite sides of the Sun for most of the apparition. Wild 2 became observable just weeks before the Stardust encounter, and, although the observing conditions were poor, we succeeded in obtaining photometry on 22 December 2003. These data confirmed that the comet was exhibiting the same behavior as was previously observed. We also obtained images of the comet on 5 January 2004, which can be used to represent the general appearance of the comet within a few days of the Stardust encounter. In this paper, we present the results from our analysis of these data.

2 Observations

2.1 Instrumentation

Observations from the 1978, 1997 and 2003/04 apparitions were obtained using the Hall 1.1-m and the 0.8-m telescopes at Lowell Observatory, while data from 1983/84 were obtained with the Perkins 1.8-m telescope at the same site. A single-channel photoelectric photometer with pulse-counting electronics was used for the photometry measurements in the first three apparitions, while a new photometer but the same phototube and electronics was used in 2003. In 1997 and 2004, images were obtained with a SITe 2048^2 CCD coupled to the Hall telescope. On-chip, 2×2 binning gave a final pixel scale of 1.13 arcsec and a field of view of 19.3 arcmin. The observing circumstances for all of our observations are listed in Table 1.

Narrowband comet filters from three different epochs were used for our observations. In 1978 the original A'Hearn and Millis (AM) set was used, although the near-UV OH, NH and continuum filters did not exist at that time (A'Hearn and Cowan 1975, A'Hearn et al. 1977). By 1983/84, the then-new International Halley Watch (IHW) set was in use, along with the older OH and NH filters, since the IHW OH filters had not yet been produced and the IHW sets did not include an NH filter (A'Hearn et al. 1979, A'Hearn 1991). The 1997 apparition occurred during the transition between the IHW filters and the new HB filters. Because the calibration of the HB filters was still in progress, we often obtained photometric data of Wild 2 using both the IHW and HB sets. For the single night of photometric measurements in 2003 a subset of the HB filters was employed.

The imaging data in 1997 and 2004 were obtained with the HB filters, along with a broadband Kron-Cousins R filter.

In each of the comet filter sets the narrowband filters were designed to isolate the emission bands of OH, NH, CN, C_3 and C_2, along with continuum points in the near-UV, blue-green and red regions of the spectrum (the red continuum filter is not used with the photoelectric system since the phototube has no response beyond about 6500 Å). We note that the bandpasses of the continuum filters have changed with each filter set, so intercomparisons of dust measurements must be made with caution. In particular, the green continuum filter bandpass moved from 5240 Å in the original AM set to 4845 Å for the IHW set and to 5260 Å for the HB set. At the same time the UV bandpass was at 3650 Å for the IHW system and at 3445 Å in the HB system, while an additional continuum filter was added at 4450 Å in the HB filter set. The differences between the specific bandpasses isolating the gas emission bands in each filter set are relatively small, and we discuss these differences in the Appendix, and also present new calibration coefficients for the AM and IHW filters.

2.2 CCD Images and Reductions

We obtained images of comet Wild 2 on a total of 10 nights between February and October 1997 and on one night in early January 2004. Exposure times for the R band images were typically 60 to 300 s depending on the brightness of the comet and 300 to 600 s for the narrowband frames. The effective seeing was typically around 3 arcsec, and the images were guided at comet rates to minimize the trailing of the comet. Basic processing of the CCD images followed standard procedures, using the CCD reduction packages in the Image Reduction and Analysis Facility (IRAF). We removed the bias and flat fielded the images, and on photometric nights we calibrated the images using Landolt fields (Landolt 1992) for the R filter and HB standards (Farnham et al. 2000) for the narrowband filters.

2.3 Photometry Observations

We followed our usual procedures in obtaining photometric observations, as detailed by A'Hearn et al. (1995). Each individual data set typically consisted of several 10–30 s integrations centered on the comet, with associated sky measurements $>0.25°$away. Various circular entrance apertures were employed, depending on the specific telescope used, the brightness of the comet and the associated sky and the need to avoid nearby stars. Standard stars were measured nightly to determine appropriate extinction coefficients and instrumental calibrations for each filter.

Photometry was obtained on a total of 21 nights over the course of the four apparitions (see Table 1). Data were obtained over a wide range of r_H, from 2.62 to 1.49 AU before perihelion, and out to 1.87 AU following perihelion. Between one and four sets of data were obtained on each night with three exceptions: On 12 and 15 February 1997, long time series of measurements were made with subsets of the filter set to look for evidence of rotational variability. As discussed later, no significant variation was detected, so the 12 February data were averaged together. On 15 February the subset consisted of only two filters, preventing us from obtaining the proper dust colors and decontamination quantities needed for the reductions, so these time series data are not included in the analyses reported here. Finally, all photometric measurements obtained on the December 2003 night were obtained in twilight and at high airmass, so only a few filters could be used, and the data have correspondingly large uncertainties. Table 2 lists the aperture diameter in arcseconds and the log of the projected radius (ρ) in kilometers for each photometric set.

2.4 Photometry Reductions

We used our basic methodology (A'Hearn et al. 1995) to reduce the photometry to absolute continuum and emission band fluxes. However, numerous details regarding the procedures and the related reduction coefficients were recently revised with the introduction of the HB filter set (Farnham et al. 2000). For the HB filter sets these issues are addressed by Farnham et al. (2000). We have subsequently back-applied these changes to the IHW, and the original filter sets and the details of this application, including revised coefficients for each of these older filter sets, are given in the Appendix of this paper. All of the data presented here have been rereduced with these new equations and coefficients so that any differences observed between one apparition and another should not be due to the specific filters used. We also note that the transmission of the original NH filter used in 1983/84 and for some of the 1997 observations suffered significant degradation with age, so appropriate corrections have been applied to the NH data obtained through this filter. Final emission band and continuum fluxes are listed in Table 2, along with an identifier indicating which filter set was used, so that the appropriate bandpasses can be associated with each of the continuum filters.

Calculations of resulting abundances and production rates for the gas species and the product $A(\theta)f\rho$, a measure of dust production, are identical to those detailed by A'Hearn et al. (1995), including the use of the same coefficients tabulated therein. Because the fluorescence efficiencies (L/N) vary with heliocentric velocity ($\dot{r}_H$) for OH, NH and CN, and with heliocentric distance for CN, the nightly L/N values are tabulated in Table 1. The resulting column abundances (Table 2) were extrapolated to total coma abundances using a standard Haser model, and the abundances were converted to production rates (Q) by dividing by the assumed lifetime of each observed species. The quantity $A(\theta)f\rho$ is the product of the dust albedo at the observed phase angle with the filling factor and the projected aperture radius. First introduced by A'Hearn et al. (1984), $A(\theta)f\rho$ is often used as a proxy for the dust production rate and will be independent of aperture size if the dust follows a canonical ρ^{-1} radial distribution and independent of wavelength if the dust is gray in color. The resulting dust and gas production rates for Wild 2 are listed in Table 3, along with the associated photometric uncertainties.

Finally, we can also compute the water production rate from Q(OH) because water is the only significant parent of OH, and the relevant parent and daughter lifetimes and velocities are reasonably well determined. To make this conversion from Haser OH daughter production rates to a vectorial equivalent water production rate, we use the empirical relation determined by Cochran and Schleicher (1993) (see also A'Hearn et al. 1995 and Schleicher et al. 1998); the results are presented in the last column of Table 3.

3 Production Rates

3.1 Heliocentric Distance Dependence

In Fig. 1 we plot the logarithm of the production rates for the five gas species and $A(\theta)f\rho$ for the green continuum as a function of heliocentric distance (r_{H}). Because our most complete coverage was in 1997 and the perihelion distance was significantly smaller in the earlier apparitions, we first focus on the 1997 data. There is a strong asymmetry for the dust, with the pre-perihelion values near log r_H=0.23 being about 2.2 times larger than at the same distance after perihelion. This change is much larger than the ~10% decrease expected from the phase effect at angles from 27° to 36° (cf. Devine 1981). This same asymmetric behavior is also evident for OH but with considerably larger photometric uncertainties. Moreover, the apparent peak in the production of both OH and NH occurs near log r_H=0.25, about 80 days prior to perihelion. While $A(\theta)f\rho$ also has its largest value at this same distance and time, the value was equally large from the beginning of our observations at about log r_H=0.28 and ΔT=−110 days. Here, however, phase effects probably are the cause of this apparent plateau, since the earliest data were obtained at phase angles of only 1°–2°and progressed to 17° on 15 February (ΔT=−80 days). Over this range of phase angle the Devine (1981) phase relation would predict about a 40% decrease in intensity, while a larger 75% decrease was measured in comet 1P/Halley (Schleicher et al. 1998). Therefore we believe this apparent static $A(\theta)f\rho$ is an artifact of the competing change with distance and change with phase angle; i.e., if the dust measurements were adjusted for phase effects to a constant phase angle, the actual peak in the amount of dust also occurred near −80 days, thereby implying that OH, NH and dust concurrently reached their maximum production approximately 11–12 weeks before perihelion. These characteristics are in sharp contrast to the results for CN, $C_2$and, to a lesser extent, C_3. For each of these carbon-bearing compounds, there is little or no evidence of pre/post-perihelion asymmetry, and the interval between ΔT=−80 and +60 days (the end of observations) shows nearly constant production rates.

Other published data sets that reveal Wild 2's behavior with heliocentric distance include longslit spectroscopy (Fink et al. 1999), hydrogen coma measurements made with the SWAN instrument aboard SOHO (Mäkinen et al. 2001) and thermal IR observations of the dust (Hanner and Hayward 2003). Fink et al. report that each detected gas species — water (based on [O I]), CN and NH — exhibit nearly constant production rates for the entire observing interval from late January to the beginning of June, while dust decreased by about a factor of 2, in generally good agreement with our results except for water. However, averaging Fink et al.'s results for each observing run, it is apparent that water production peaks in early March and drops to less than 60% of the peak by early June, unlike their near-flat CN production. Thus their water behavior is a closer match to our OH results than might be inferred from their text. Water production rates from the SWAN hydrogen measurements (Mäkinen et al. 2001) have high uncertainties and are consistently nearly twice as high as our OH results but also exhibit a significant decrease between late March and mid-July that is qualitatively similar to our OH data. In the case of the dust, in addition to the factor of 2 drop measured by Fink et al., Hanner and Hayward's thermal IR data show a three-fold drop in dust production between February and August, with their rate of change consistent with the Fink et al. data set as well as our own.

In conclusion, there appears to be unanimity regarding the dust decrease with time starting months prior to perihelion and consistency with the similar trend of water, although with much greater uncertainties for all data sets. Minor species, however, such as CN, exhibited near-constant production over similar time frames. A natural explanation is that the early production peak and asymmetry in water and dust production are consequences of a strong seasonal effect with at least one source region moving rapidly from summer to winter, similar to what was observed for comet Borrelly (Farnham and Cochran 2002, Schleicher et al. 2003). The different behavior of the minor species, other than NH, could imply heterogeneities in the chemical composition among different source regions.

3.2 Comparisons Among Apparitions

Although we have data from four apparitions, there is, unfortunately, very little overlap in the observational circumstances among the apparitions. For instance, the only pre-perihelion, large $r_{\rm H}$ observations were obtained during the 1983/84 apparition, while no small $r_{\rm H}$ data were obtained in 1984 because the comet had a small solar elongation. Generally, the 1983/84 production rates appear somewhat higher than might be expected from an extrapolation of the 1997 data, though relatively large uncertainties and the unusual $r_{\rm H}$-dependent behavior make this trend inconclusive. The only data we obtained at large $r_{\rm H}$ after perihelion were from our one night in 2003. These measurements will be discussed in more detail in Section 5, but the CN and C_2 are consistent with simple extrapolations of the 1997 post-perihelion results, while the nominal dust production is higher than would be predicted.

We do have observations essentially at perihelion in both 1978 and 1997, but q changed by 0.11 AU between the two dates. Intercomparing these perihelion data, it is clear that the 1978 gas measurements are significantly (2–3 times) higher than would be expected by any reasonable extrapolation from the 1997 data set, while the dust in 1978 was only somewhat higher than might be expected. Though inconclusive, we consider this behavior possible evidence of an evolutionary effect associated with Wild 2's first approach to the Sun after its orbit was perturbed in 1974. This interpretation is not clear cut, however, because the only other observations from 1978, at $r_{\rm H}$=1.80 AU, are a fairly good match to the 1997 measurements at the same distance.

Because of the unusual behavior of $Q(r_{\rm H})$, the standard procedure of calculating the power law slope for each species is nearly meaningless, particularly with the maximum production rate being reached nearly 3 months prior to perihelion (at least during the 1997 apparition). Therefore we have performed this calculation only for CN, where the data in log-log space appear most linear and the associated photometric uncertainties are small. Including all observations from the 1997 apparition yields a slope of -2.61 ± 0.44, while combining the first three apparitions gives a slope of -2.68 ± 0.32 (and an associated offset of the intercept from the 1997-only fit). While these slopes are slightly steeper than would be expected solely from the change in available solar radiation with $r_{\rm H}$, they are completely consistent with those from many other Jupiter-family comets (A'Hearn et al. 1995)

3.3 Composition

The relative abundances are listed in Table 4, as defined by the average ratio of each species' production rates with respect to OH from Table 3. In each case the average is simply the unweighted mean ratio. The resulting log of the C_2-to-CN production rate ratio — the primary discriminator in compositional classification (A'Hearn et al. 1995) — is -0.37 ± 0.18. However, because OH was not measured in 1978, nor for five of the data sets in 1997 (four of which were obtained prior to the delivery of the HB OH filter), nor for the three sets obtained at high airmass in 2003, these OH-based ratios do not incorporate all observations. As a check, we therefore also directly computed the log of the C_2-to-CN production rate ratio, -0.34 ± 0.17 (excluding the consistent but high uncertainty value from 2003). We also examined each direct C_2-to-CN value as a function of apparition and $r_H\dot{N}$o trends are evident with either parameter, so we conclude that this primary measure of Wild 2's composition has remained constant over time and with distance from the Sun, an unsurprising result given the similar orbital behavior of each of the carbon-bearing species. As discussed recently in papers about Comets Hyakutake (1996 B2) (Schleicher and Osip 2002) and 19P/Borrelly (Schleicher et al. 2003), a direct comparison of abundance ratios with the taxonomic classes determined from the A'Hearn et al. (1995) database must be made with caution, because of changes in filter reduction coefficients related to our improved understanding of the shape and extent of the wings of the C_2 and C_3 emission bands (see the Appendix and Farnham et al. 2000). To first order, these changes will result in new C_2-to-CN ratios ~17% larger than would have been computed previously, but the specific shift also depends somewhat on the dust-to-gas ratio of a particular comet. Although the entire photometric database will eventually be rereduced, one can reasonably estimate from Table VI from A'Hearn et al. and the 17% shift that the log of the mean C_2-to-CN production rate ratio for "typical" comets is approximately +0.13, and the division between the typical class and the depleted class is approximately −0.11. Thus Wild 2's value of −0.34 (or −0.37) places it in the carbon chain-depleted class, about a factor of 3 below the mean value of the typical classification, with slightly greater depletion than measured for comet Borrelly by Schleicher et al. (2003).

Direct intercomparison of abundance ratios from different data sets is complicated by the usage of differing g-factors and/or scalelengths among various researchers. Despite this, there is consensus that C_2 is depleted with respect to CN by both Cochran et al. (1989) and Fink et al. (1999) on the basis of upper limits for C_2 detections and by Schulz et al. (2003) from a single observational set. We note that our success in acquiring detections of the C_2 emission throughout the apparitions is due to the much larger aperture sizes we typically use as compared with aperture or long-slit spectroscopy, greatly improving the overall contrast of the emission bands to the underlying continuum, since the radial profile of the continuum generally drops off much more rapidly than the observed gas species.

Finally, because both the OH and the dust exhibit similar behavior with heliocentric distance, there is essentially no trend in the dust-to-gas ratio with time. As listed in Table 4, the log of the ratio of $A(\theta)f\rho$ (green continuum) to Q(OH) is −25.28 cm s molecule^{-1}, which is larger than the average for all comets but in the mid-range for comets in the depleted class (A'Hearn et al. 1995).

3.4 Water production

Using the conversion method mentioned in Section 2.4, we compute the vectorial-equivalent water production rates from the Haser model OH production rates, and the results are listed in the final column of Table 3. The peak water production rate, approximately 1.1×10^{28} molecules s^{-1}, is much lower than the 3×10^{28} molecules s^{-1} predicted by Osip et al. (1992) from a simple extrapolation of the large r_H 1982 observations. However, the 1997 photometry clearly show that OH (and water) production does not follow a simple power law $r_H$dependence, and this results in the large discrepancy between the Osip et al. prediction and our measured peak water production. Our measured peak water production implies a maximum effective active area of about 6 km^2, based on the Cowan and A'Hearn (1979) water vaporization model and an assumed isotropic source function. As will be evident from later discussions about the pole orientation and source location, however, the actual active area is likely to be somewhat smaller than this.

Our water production rates are somewhat lower than those found by Fink et al. (1999) and nearly a factor of 2 lower than those of Mäkinen et al. (2001). While each data set has relatively large uncertainties, and both Fink et al. and Mäkinen et al. warn about the difficulties in background removal (spectral and spatial, respectively), it is not apparent why systematic offsets should result. The only other water measurement of which we are aware is from the radio OH database of Crovisier et al. (2002). They give a single composite value of 7×10^{27} molecules s^{-1} from observations between 21 January and 23 April 1997, which is entirely consistent with our measurements during this interval.

3.5 Dust Colors

Our analysis of the color of the dust grains is limited to the 1983/84 and 1997 apparitions because they are the only ones for which reliable continuum measurements were obtained at two or more wavelengths. In Fig. 2 we plot the differences in log $A(\theta)f\rho$ values between pairs of continuum filters as a function of heliocentric distance. These plots show no evidence of any trend in the dust colors either with $r_{\rm H}$ or with time from perihelion, in spite of the strong asymmetry around perihelion in the apparent dust production. The dust colors, in units of $\Delta(\log A(\theta)f\rho)$, are readily converted to a percentage reddening per 1000 Å, although the different location of the UV and green continuum points for the IHW and HB filters must be accounted for in this computation. Unfortunately, there is a large amount of dispersion among the individual color measurements due to the large uncertainties in many of the UV continuum measurements. In fact, including all 25 data sets that have both a green and UV continuum measurement yields an unweighted average percentage reddening per 1000 Å of 74%±88%. Including only the 12 data points for which the photometric uncertainties of the UV continuum were less than 25% yields an average reddening of 36%±23% per 1000 Å.

We can also examine the color between the blue and green continuum points for the HB filter set. For the 11 data sets from 1997 the reddening between 4450 and 5260 Å is 20%±10% per 1000 Å, a result that is still not tightly constrained. Overall, we would classify Wild 2 as having moderately reddened dust. These results can be compared with the colors determined by Schulz et al. (2003) on 2 and 3 April 1997 from broadband BVR images (13.1%±3.0% per 1000 Å) and from continuum points within longslit spectra (6.2%±5.0%), and colors extracted from the reflectance spectra plotted by Fink et al. (1999) (9–16% per 1000 Å between 5300 and 9800 Å for three observing runs; see their Fig. 1). Taken together, it appears that the dust is more strongly reddened in the near-UV than at longer wavelengths.

4 1997 CCD Image Analysis

4.1 Coma Morphology

Comet Wild 2 has an orbital inclination of only 3°, so the Earth always lies very close to the comet's orbital plane. Furthermore, throughout our February, March and April 1997 observations, the Earth-comet observing geometry remained relatively constant, with only a 14° change in the ecliptic longitude. These circumstances allowed us to observe inherent temporal changes in the comet with little confusion from changing perspectives. From July through October, more dramatic changes occurred, with the ecliptic longitude changing 50° between April and July and another 50° by October.

Our images from February through July (Fig 3) reveal a number of different features. The central coma is elongated in the sunward-antisunward direction, and at larger distances a faint anti-tail can clearly be distinguished. Synchrone and syndyne analyses suggest that this anti-tail is the result of large, slow-moving particles emitted several months before perihelion (probably around the time of peak activity). From February through April a broad ($\sim 50^\circ$–60° FWHM) fan extends to the northeast. Because this feature is oriented nearly perpendicular to the projected orbital plane, it must be produced by directed emission rather than by radiation pressure. Not only does this fan (which we designate the primary jet) show no apparent changes over an 8-hour period on 14 February, it exhibits little change on weekly or monthly timescales from February through April. (Table 5 lists the measured position angle and width of the fan in our observations.) Given the constant viewing geometry and unchanging appearance of the fan, we conclude that the fan itself must remain nearly unchanged during this time period. Finally, a dust tail is present in most of our images at a projected position angle (PA) around 100°. This tail is essentially absent in early February, most likely because the solar phase angle is small and the tail is pointed away from Earth, but becomes more visible as the phase angle increases.

By 9 July, our 1997 observation closest to the Stardust encounter distance (+63 days, where Stardust encounter was +98 days), the fan has faded, and a new sunward pointing jet has appeared. We conclude that this jet is different from the fan jet because it points south of the orbital plane, while the fan always pointed north. The secondary jet is also narrower and more sharply defined than the fan, even though the comet is nearly twice as far from the Earth as it was in the earlier observations. When emerging from the central condensation, the jet appears to point almost directly sunward, but at larger distances it curves toward the tail. This curvature could be due to rotation of the nucleus or to radiation pressure pushing the material into the tail. Another feature that is clearly seen in the July data is a well-defined parabolic envelope on the sunward side of the coma. In September and October the coma is elongated as it was earlier but otherwise exhibits no well-defined features, which may not be surprising, given that the geocentric distance has increased to 2.7 AU.

4.2 Rotation State Analysis

Many of our observations during the 1997 apparition were focused on trying to determine the rotation state of the nucleus (rotation period, spin axis orientation, etc.). During our 14 February and 5 March observations, we made frequent observations of Wild 2 over 8- and 5-hour time spans to look for variability in the comet's lightcurve. Because of the high activity level at this time, the coma overwhelms the signal from the nucleus, so any variation that might be observed would be due to the changing production rates as an isolated source region rotates into and out of the sunlight.

We performed aperture photometry on our images, using a 4-arcsec radius aperture to maximize the S/N, while minimizing the effects of seeing and the dilution of the lightcurve amplitude by the older coma material. The comet and several field stars of varying brightness were measured in each image, and the field stars were used to perform a first-order correction for the differing amount of extinction in each frame to correct for thin cirrus that was present in many of the observations (see Farnham 2001 for more details). Figure 4 shows the resulting lightcurve of comet Wild 2, along with two comparison stars, from 14 February. Though there seems to be a slight difference between the first and second halves of the night, there is also a change in the S/N ratio between the two halves, indicating that the sky conditions were changing during this time. From these results, and those from 5 March, we found no clear brightness variations at a level of 0.05 mag, and certainly no variations that suggest a periodic modulation produced by rotation of the nucleus.

The lack of measurable variability in our lightcurves limits our ability to determine the rotation period of the nucleus, however; we can utilize the behavior of the production rates and the jet morphology to explore other properties of the comet's rotation. First, the production rates peak in February, about 3 months before perihelion, and then begin to drop around perihelion, even though the solar irradiation is increasing. This seasonal activity, combined with the lack of short-term variability, suggests that there is an active area that is nearly constantly illuminated during February but then turns away from the Sun as the comet passes perihelion. Second, the constant appearance of the fan jet from February through April and the fact that it remains roughly perpendicular to the comet's orbit suggest that the fan is always pointed in the same direction in an inertial coordinate system. To explain these observations, we conclude that the nucleus has an active region on or near its rotation pole, and the emissions from this source form a cone around the pole as the nucleus rotates. Viewed from outside, this cone is seen as the long-lived fan centered on the projected rotation axis. Finally, the fact that the fan remains unchanged on timescales of hours, days and months, combined with the repeatable activity levels from one orbit to another (from our photometry results and the magnitude measurements of Sanzovo et al. (2001)), suggests that the nucleus is in a state of simple rotation. There is always the possibility that the nucleus has some complex rotation or long-term precession, but any potential effects from these factors are not evident in our data. Therefore, for our analysis, we adopt the assumption that the nucleus is most likely in a state of simple rotation.

Knowing that the fan is centered on the spin axis allowed us to determine the orientation of the pole using the same technique used for comet Borrelly (Farnham and Cochran 2002). Assuming that the center of the fan represents the projected spin axis, we measured the apparent PA of the fan in each image. We then performed a grid search of pole positions, computing the expected PAs for each of our measurements in each case. Using a least squares fit, we searched for the pole position that best fit our observations.

There are some minor complications involved with the application of this technique in this particular instance. First, the fan is somewhat broader and more diffuse than the jet observed in comet Borrelly and sometimes shows curvature at larger distances, which occasionally affects the PA measurement. Second, in some of our later images the dust tail lies at the edge of the fan, and this proximity may skew the measured position of the center of the fan. Finally, if the active area is not centered on the pole, then as the sub-solar latitude nears the equator, the source may rotate into and out of sunlight, at which time the center of the fan may not truly represent the position of the spin axis. Although each of these complications likely introduces an uncertainty of a few degrees, there are other factors that mitigate the problems. First, the observing geometry changes little through many of the observations, so measurements from multiple images can be used to reduce the uncertainties. Second, the early February images show a well-defined fan, and measurements from these times are not skewed by contamination from the dust tail. Finally, to reduce the problems with curvature of the jet and the interference from the dust tail, we measured the PA at several different distances from 5 to 15 pixels (∼6–17 arcsec), allowing us to characterize any curvature and determine the PA as the jet is followed in to the optocenter.

Figure 5 shows our best fitting pole solution of α=281°±5° and δ=+13°±7° (J2000). (In ecliptic longitude and latitude, λ=283° and β=+36°. In orbital plane coordinates the obliquity and orbital longitude are 56°±7° and 103°±6°, respectively, where the longitude is measured along the orbital plane in the direction of the comet's motion, from the anti-solar direction at perihelion.) For our discussion we define this to be the north pole. We note that our solution is very close to that found from the orientation of the nucleus' short axis (290°, +13°; Brownlee et al. 2004). Using our solution, we computed the sub-solar and sub-Earth latitudes as a function of time (Fig. 6), and we can use this information to explore times that the sources are likely to be active, thus helping to constrain their latitudes. If we assume a spherical nucleus, the pole enters continuous shadow on 29 May. The fan's typical width of 50°–60° suggests that the primary active area is likely to be within about 15° of the pole, or at a latitude higher than +75°. An active area north of +75° should then start to shut down during part of the rotation around mid-April and should have shut down completely by mid-June. Unfortunately, we have no observations between 25 April, when the primary jet is present, and 9 July, when it is completely gone. Thus, although our observations are consistent with a source north of +75°, they cannot be used to constrain the location any more tightly than this.

If we assume that the sub-solar latitude must be within 90° of the source latitude for the jet to be active (i.e., the source is illuminated for at least part of a rotation), we can use the times at which the secondary jet is active to put some limits on its location. We see no sign of the secondary jet in any of our images from February or March, even though we have frequent observations at irregular intervals. We also know that there were no variations detected in any of our lightcurves during this time, suggesting that the secondary jet was not turning on and off. If we adopt the most severe limit, we conclude that the source was in continuous darkness at least through 1 February, when the sub-solar latitude was at +53°. This sets a strong northern limit of −37° for the location of the secondary. If we adopt a less severe, yet still reasonable constraint, and allow that the jet did not turn on until after 1 March, when the sub-solar latitude was at +41°, this constrains the location to a latitude south of −49°. To limit the southernmost allowable position of the source, we use the earliest date on which the jet was observed to be active. Our only image showing the secondary jet is from 9 July, but Schultz et al. (2003) obtained an image on 2 April that also seems to show a secondary jet (we discuss these data in more detail in Section 4.4). If the jet is active at this time, when the sub-solar latitude is at +28°, then the secondary must be at a latitude north of −62°. Thus we conclude that the secondary source must be at a mid-southern latitude, between −37° and −62°, with a more probable location between −50° and −60°.

We can present several additional, though more circumstantial, pieces of evidence that support our pole solution. Changes in the sub-solar latitude provide a qualitative explanation for the observed behavior in the production rates. The Sun reaches its most northerly latitude of 56° at the start of December 1996, so the primary active area is fully illuminated throughout the February–March time frame as the comet nears the Sun. The trade-off between increasing solar irradiance and decreasing altitude of the Sun (as seen from the north pole) is qualitatively consistent with the observed peak in water and dust emission in February. By the time Wild 2 reaches perihelion in May, the primary source is nearly in continuous shadow, and the production rates drop, to be dominated by the secondary source after perihelion. The pole orientation also explains the lack of variations in the lightcurve during our February and March observations. During this time the Sun is at latitudes above +40°, which means it is continuously illuminating the primary active region, so there is no modulation of the activity from that source and hence no variation in the lightcurve.

To determine the direction of spin of the nucleus, we turn to the secondary jet, which exhibits curvature in the image of 9 July (see Fig. 3). In the innermost region of the jet the curvature follows a gentle spiral shape, while farther out, it rapidly becomes more severe and nearly bends back upon itself. The outer part of the curvature is clearly caused by radiation pressure turning the dust grains away from the Sun, while the curvature in the innermost region, which can be traced all the way in to the central condensation, appears to be caused, at least in part, by outflow from a rotating nucleus. If this is indeed the case, then the anti-clockwise direction of the curvature defines the sense of the nucleus' spin. On 9 July our pole was at a projected PA of 76°, with an aspect angle of 81°, so the curvature of the secondary jet means that the quoted pole direction is indeed the dynamic north pole, as defined by the right-hand rule. (Detailed modeling of this jet may ultimately provide constraints on the rotation period, but this is beyond the scope of this paper.) Our derived rotation properties and jet locations are summarized in Table 6.

4.3 Coma Analysis

The 9 July image shows a well-defined, parabolic envelope, centered on the sunward direction. The coma inside the parabola falls off with the canonical slope of -1 and then, at the projected distance of 2.4×10^4 km, drops very rapidly to the sky level. These are classical qualities of a fountain model, in which the grains are being turned back into the tail by radiation pressure at a characteristic standoff distance (Grün and Jessberger 1990; Baum et al. 1992). We can take advantage of this coma structure to estimate the velocity of the dust grains at the point where they decouple from the gas flow. The relationship between the standoff distance, D (km), the grain radius, a (μm), and the terminal velocity of the dust (when it is no longer being accelerated by gas drag), v_o (km s^{-1}) is given by

$$D = \frac{1.45 \times 10^5 a \rho v_o^2 r_{\rm H}^2}{\sin \alpha}$$

, where ρ (g cm^{-3}) is the grain density, $r_{\rm H}$ (AU) is the heliocentric distance, and α is the solar phase angle. For the 9 July observations, D=2.4×10^4 km, $r_{\rm H}$=1.703 AU, and $\alpha = 34.8°$, so this relation reduces to $a\rho v_o^2$=0.0326. Without any constraints on these three parameters, we cannot solve for the others, but we can look at the families of solutions as plotted in Fig. 7. Since we observed with the R filter, we can assume that the optically important grains are a few microns in size, so the velocity should be around 0.1 km s^{-1}. To get a more specific solution, we can adopt the optically important grain radius of 1.7 μm that was derived by Sanzovo et al. (2001) for a particle with ρ=1.0 g cm^{-3}, which gives a dust velocity of 0.14 km s^{-1}. For grains of increasing fluffiness the velocity will be somewhat higher, as radiation pressure acts more efficiently on lower-density particles.

We can explore spatial variations in the coma by taking a ratio of two images (after subtracting the sky and aligning the optocenters), which will highlight any differences between the two frames. If the images were taken at different times, then the ratio reveals temporal changes that have taken place during the interval between the two observations. Alternatively, if the two images were obtained at about the same time but at different wavelengths, then the result will show any color differences in the coma. For the temporal analysis we have two nights in which the observations span several hours: 14 February (7 hours) and 5 March (4 hours). For the color analysis we have four nights in which data were obtained with two or three narrowband continuum filters: 14 February

(4450, 5260 and 7128 Å), 5 March (5260 and 7128 Å), 25 April (5260 and 7128 Å) and 9 July (4450 and 5260 Å).

The results from the temporal analysis show no measurable changes in the coma, either on 14 February or on 5 March, indicating that at these times the coma was essentially unchanging on timescales of several hours. This should be expected if the primary source is actually located at the pole, but if the source is truly offset by 10°–15°, then the lack of temporal changes probably indicates that the rotation period is significantly longer than the 4- or 7-hour time span covered by these sequences. The results from the wavelength analysis are similar, showing no spatial color variations in any combination of filters. This suggests that the dust in the jets has essentially the same particle size distribution (PSD) as in the rest of the coma (and, indeed, lateral diffusion of particles out of the jet may be the source of much of the dust in the rest of the coma). Unfortunately, we have no measurements that allow us to determine whether or not the primary and secondary jets have the same PSD.

In addition to the dust images, we also have images obtained with narrowband filters that isolate the emission from CN, C_2 and C_3, the best of which were obtained on 14 February and 9 July. Unfortunately, standard star measurements are not available to provide a proper flux calibration of the images on 14 February, the better night of the two, so we can only perform a crude continuum removal to look at the basic morphology of the gas coma. A master dust image, created by averaging several continuum frames, is aligned with the optocenter of the underlying dust in the gas frame, scaled to the appropriate brightness (so that when the continuum is removed, the remaining gas coma remains smooth across the optocenter) and subtracted from the gas image to leave the pure gas morphology. Proper calibration and continuum removal (Farnham et al. 2000) were done for the 9 July data. The pure gas images from both 14 February and 9 July show essentially round comae with no significant structure. On 14 February a slight asymmetry, in the direction of the primary jet, can be seen when an azimuthally averaged profile is removed, but the 9 July data show no such asymmetry. Other enhancement techniques reveal no additional structure on either date.

Finally, we used the surface brightness of the coma to investigate the dust production, both in terms of $A(\theta)f\rho$ and in real mass production rates. First, for our calibrated CCD data, we used aperture photometry to measure the brightness of the coma in different apertures and computed the value of $A(\theta)f\rho$ using the same procedures that were applied in Section 2.4. Comparing the results for comparable apertures from our images on 5 March and 9 July with those from our photometry on 5 March and 3 July, we find nearly identical results (479 cm for the March images, 457 cm for the March photometry, 195 cm for the July images and 200 cm for the July photometry), providing confirmation that measurements from the different instruments are consistent. We then compared the 9 July result with the $A(\theta)f\rho$ from 1 October and found that it had dropped only from 195 to 157 cm during this interval. Because these two observations bracket the corresponding point at which the Stardust encounter took place, and because the activity is essentially repeatable from one orbit to another (on the basis of our photometry and the results of Sanzovo et al. (2001)), we conclude that our 9 July observations should be a reasonable representation of the conditions at the time of the encounter.

With this in mind we estimated the mass production rates of the optically important dust grains, adopting the technique used by Farnham and Davies (2003). The surface brightness of the coma, B (erg cm^{-2} s^{-1} Å^{-1}) is related to the dust production rate, $\dot{M}$ (g s^{-1}) via

$$\dot{M} = 3.750 \times 10^{23} \frac{\Delta^2}{p_o^2} \frac{r_{\rm H}^2}{S_0} \frac{B\, a\, \rho\, v_o\, R_o}{A},$$

where Δ and $r_{\rm H}$ are the geocentric and heliocentric distances to the object (AU), p_o is the pixel size at the distance of the object (km), S_0 is the solar constant at 1 AU, a is the dust grain radius (μm), ρ is the grain density (g cm^{-3}), v_o is the velocity of the dust (km s^{-1}), R_o is the distance from the nucleus projected onto the sky (km) and A is the dust albedo. Again, we adopt the Sanzovo et al. (2001) grain size of 1.7 μm, our corresponding velocity measurement of v_o=0.14 km s^{-1} and reasonable values of ρ=1.0 g cm^{-3} and A=0.05. For the solar constant we use 190, 187 and 120 erg cm^{-2} s^{-1} Å^{-1} for the blue, green and red continuum filters, respectively. Δ and $r_{\rm H}$ are listed in Table 1, and the pixel sizes, p_o, are 723 and 1388 km for the 5 March and 9 July images, respectively (from which R_o can be computed for a given pixel). In principle, we could apply this relation to the surface brightness at any point in the coma to obtain a measure of the production rate. However, if the dust does not follow a ρ^{-1} falloff, then different results will be obtained at different distances. Similarly, the production rates measured in a jet are likely to be different from those in the quiescent parts of the coma. Thus we implement a more systematic method by which we compute the mass production at different distances in a given azimuthal direction, so these changes can be evaluated.

To generate a radial profile of the surface brightness for a given azimuthal direction in the coma, we use a wedge that overlies the area of interest, with its apex at the optocenter. For each distance along the wedge all pixels are averaged together to produce the averaged radial profile. These surface brightness profiles are then converted to mass production rate profiles using the above relation. If the dust outflow is purely radial, then the production rate profiles will be constant for all distances; however, if the derived production rates are seen to change with distance, then the outflow deviates in some manner, either because of the effects of radiation pressure or because of some changing properties of the grains (fading, fragmenting, etc.). The advantage of using the radial profile technique, however, is that we can use the radial behavior to extrapolate to zero distance, where the surface brightness is affected by seeing, tracking and centering issues, to determine the production rates at the nucleus. Our derived mass production rate profiles are shown in Fig. 8. For 5 March the wedges were centered on the primary jet at a PA of 22°and a quiescent region at 270°, and the 9 July profiles were obtained along the secondary jet at 275°and on the quiescent region at 0°.

Figure 8 reveals some interesting items regarding the two observation dates. First, it is clear that the primary jet is more active in dust production than the secondary jet. Extrapolating the two jet profiles in to zero distance, we find that the primary emits dust at a rate of 23 kg s^{-1} on 5 March, while the secondary is at 9 kg s^{-1} on 9 July. This is consistent with our photometry results that show higher production rates when the primary jet is in sunlight and lower rates when the secondary is active. Even though the solar insolation available to drive the activity is the same in both cases (in March the comet was at $r_{\rm H}$=1.7 AU inbound, and in July it was at 1.7 AU outbound), the activity levels are also affected by the local solar altitude and by the rotational modulation of the secondary jet. Thus, even though the secondary jet has a lower *average* production rate, we do not have enough information to make any solid conclusions about the relative sizes of the two sources.

Another item of interest is the behavior of the surface brightness as a function of distance from the optocenter. In March the curves drop with distance, following a $\rho^{-1.33}$ relation, whereas the July curves show essentially constant production rates, at least out to the point where the envelope rapidly drops to the sky level at 15–20$\times 10^3$ km. Furthermore, the quiescent region of the coma in each case mimics the shape of its corresponding jet profile. This suggests that some, if not all, of the material in the ambient regions of the coma comes from grains that were originally emitted in the jet and either diffused out laterally or were pushed out of the jet by radiation pressure. In the March profile the quiescent region is only about half as bright as the primary jet, whereas in July the quiescent coma is about 60–70% of the secondary jet brightness. This difference may be caused by the mechanism that is removing grains from the jets, or it may indicate that part of the dust (2–3 kg s^{-1}) comes from an underlying isotropic component or from other unresolved sources.

4.4 Comparison with Other Published Results

Pittichova and Meech (2001) obtained lightcurve measurements on four different observing runs when the comet was far from the Sun, in an attempt to observe the rotation of the bare nucleus. On the first three runs, no significant variations were seen, and, given our pole solution, we suggest that this was due to unfavorable viewing geometry. During all three runs, the Earth was at high cometocentric latitude (November 1996, $+54°$; June 1998, $-44°$; and September 1998, $-50°$), a configuration that would minimize the changing apparent cross section of the rotating nucleus. On their fourth run in August 1998, conditions were better, with the Earth at $-23°$ latitude. On this run some night-to-night variations were detected, but with no obvious periodicity.

We can use our pole solution to predict the best times at which to look for rotational variation. Typically, there are two optimum times for measuring the comet's lightcurve variability. The first is when Wild 2 is inactive and the Earth is near its equator (for recent apparitions, this occurs shortly after aphelion), so the bare nucleus displays the most extreme cross sectional changes as it rotates. The Stardust images show a nearly triaxial nucleus, with radii 1.65$\times$2.00$\times$2.75 km (Brownlee et al. 2004), so lightcurve variations of a few tenths of a magnitude should be measurable. The other optimum is shortly after perihelion, when the primary jet is inactive and the secondary source is periodically turning on and off. As far as recent apparitions, September 1994 presented good circumstances because the comet was not only near aphelion, but was also near opposition, so any existing measurements from that time frame could show rotation of the bare nucleus. Shortly after perihelion in June 1997, the comet was visible for only a few hours each night, but observations at this time may show night-to-night variations and could be useful in determining if the rotation period is several days. Unfortunately, the two most recent opportunities, in March 2001 (aphelion) and October 2003 (perihelion), both took place when the comet was near solar conjunction, severely limiting the ability to obtain a lightcurve. Fortunately, the next two possibilities present highly favorable circumstances. The Earth will cross Wild 2's equator in October 2007, at which time the (inactive) comet will again be near opposition and will be visible for many hours each night. After that, the comet will again pass perihelion in February 2010 in an excellent apparition for observations. Not only will the comet be near its closest point to the Earth in April (0.67 AU), but throughout much of the year it can be observed for at least 4 hours nightly, with the possibility of up to 10 hours of observing time in April and May (when the sub-solar point is at southern latitudes on the comet). This offers an ideal opportunity to look for variations in the coma brightness on timescales of hours, days and months.

Schulz et al. (2003) obtained data on four observing runs from 1996–1998. Unfortunately, when processing the images presented in that paper, the authors used the "surfphot" utility from the MIDAS package, which is designed for analyzing galactic profiles. This routine fits concentric elliptical isophotes to the coma, allowing the axial ratios, the direction of elongation and the centers of each ellipse to vary independently from their neighbors. Although it is valuable for measurements of galactic profiles, this routine causes problems when it is used as an enhancement technique for comets because the ellipses that are being removed contain much of the important information about the coma (i.e., the very information that is considered meaningful in the galactic profiles is being removed from the comet's coma morphology). By fitting to the coma shape, the ellipses are offset toward the brighter features (the primary jet, for example), causing those features to be severely suppressed in the final result, or, if the features are elliptical in shape, they can be removed altogether. Similarly, the fainter regions of the coma will be strongly overemphasized, so the relative brightness of different features (or even different parts of the same feature) in the enhanced image is meaningless. Furthermore, because each concentric ellipse has a different axial ratio, a different direction of elongation and a different offset from the optocenter, this technique has the strong potential for shifting the locations of any features that are seen in the enhanced image, making any position measurements questionable. Finally, comparison of two enhanced frames is difficult because images exhibiting different coma features raise the question of whether the difference is due to the inherent morphology or to the profiles that were removed.

With these qualifications in mind, we can explore the Schulz et al. images with respect to our results. First, the 11 September 1996 and 31 March 1998 data show no dramatic features, though the primary jet, in its early stages of activity, may be faintly visible to the north in September. Both the 11 December 1996 image and the 2 April 1997 image (rotated 180° from the others) show the primary jet extending to the northeast. Inspection of the published images shows that the PA of the jet is around 30–35°in December and about 15–20°in April. These are offset slightly from those predicted by our pole solution — 41° and 35°— but with the uncertainties introduced by the processing, we believe they are consistent with our results. This is especially true since the jet in our 31 March image (obtained just 3 days before their 2 April image and enhanced with our more benign techniques) has a PA that fits well to the predicted value.

The 2 April image also shows the dust tail and the secondary jet. As we saw no sign of it on 31 March, this jet must be intermittently active, most likely because of rotation of the nucleus. The presence of the secondary jet at this time means that its source must be receiving sunlight, which allowed us to constrain its latitude (section 4.2). We note that because the primary jet and dust tail are bright, the elliptical coma profiles were pulled to the northeast (the middle panel of their figure 1 shows the offset) and the secondary jet was overenhanced. This enhancement makes the secondary appear brighter than the primary jet, even though the original image clearly shows that it is really much fainter. In the unenhanced image, there also appears to be an extension in the coma at about 170° PA, yet this extension has been completely removed in the processed version.

Sekanina (2003) used the Schulz et al. (2003) images to derive some of the comet's rotational properties. In general, his results agree well with ours, though quantitatively there are differences. Sekanina found a spin axis orientation of α=297°, δ=−5°, which is different from our solution by 24°. We note that his pole solution does not fit well to our data, predicting the jet should be at a PA of 0° to 10° during February and March when we consistently see it at ∼30°. The difference of our results from Sekanina's likely arises from the fact that he used only two images, the minimum required to compute a solution, and the measured positions from those images may be questionable. Another difference between the two results is the location of the secondary source. Sekanina places it at $-25°$, while we find it to be between $-37°$ and $-62°$. Since both results were determined from the time at which the secondary turned on, this discrepancy can be attributed entirely to the differences in the pole solutions.

5 2003 Apparition

The poor observing geometry for Wild 2's 2003 apparition precluded any ground-based optical observations from early June through late December because of the comet's being in solar conjunction, and when Wild 2 did emerge, it was far from the Earth and fading rapidly. However, in support of the Stardust encounter, we obtained narrowband photometry as early as possible before the flyby. The results of these measurements, discussed below, were communicated to the Stardust team prior to their deadline for last-minute adjustments to the closest approach distance of the spacecraft. We also obtained images of the comet 3 days after the encounter to help in interpreting the spacecraft observations.

Stardust had a successful encounter with comet Wild 2 on 2 January 2004 (98 days after perihelion), obtaining high-resolution images of the nucleus, taking measurements of the dust environment and collecting dust grains that will be returned to Earth in 2006.

5.1 Implications for the Stardust Encounter

On the basis of our preferred pole solution, at the time of the Stardust encounter the sub-solar latitude was at $-32°$, and the sub-Earth latitude at $-44°$, so the primary source was in continuous darkness and inactive. This fact increased the likelihood of a safe flyby, as the dust production was lower than it would have been otherwise. We do not have enough information to determine if the secondary jet was active or not at the time of closest approach, but with its mid-latitude location, the source would be well illuminated at local noon. Fortunately, the mass production rates shown in Fig. 8 indicate that the column density through the secondary jet is only 50–60% higher than in the ambient regions of the coma, so the total amount of dust encountered on a path through the jet would not differ dramatically from paths through other parts of the coma (though the spatial density and/or size distribution of particles in the innermost coma may be different).

A cursory inspection of the Stardust images (Newburn et al. 2004, Brownlee et al. 2004) shows many well-defined jets; however, no single jet is significantly brighter than the others, so it is not obvious which, if any, of them is the secondary seen in our images. It is reasonable to assume that our secondary jet is more active than the others seen in the Stardust images, which raises the issue of whether it was not fully illuminated at the time of the observation. The analysis of the Stardust jets by Sekanina et al. (2004) shows a number of sources at middle latitudes, with four of them (ρ, μ, τ, ν) clustered together near the terminator. It is possible that one or more of these is our secondary source, and it is simply not receiving enough sunlight to make it stand out from the others. (We note that the Sekanina et al. analysis was done for a slightly different pole orientation than ours, but it is close enough that the range of possible source locations is still comparable.)

5.2 Photometry Measurements — December 2003

We obtained narrowband photometry during morning twilight just 12 days before the Stardust flyby. Although only three gas measurements were successfully obtained — two for CN and one for C_2 — and the uncertainties are quite large because of the rapidly brightening background sky, these points are consistent with pre-perihelion data at the same heliocentric distance, as we would expect given the lack of asymmetry observed for CN and C_2 at earlier apparitions. This result indicates that Wild 2's gas production was normal just prior to the encounter, so we believe that our original prediction for the water production at the time of the Stardust encounter probably remains the best estimate for the total gas production at that time. This value, $4(\pm1)\times10^{27}$ molecules s^{-1}, is based on an extrapolation of the post-perihelion OH measurements from 1997. Again applying the Cowan and A'Hearn (1979) vaporization model, this would correspond to an effective active area of about 2–3 km^2. Given the size of the nucleus, $1.65\times2.00\times2.75$ km (Brownlee et al. 2004), this implies a fractional active area of about 5–8% for all sources active around the time of the encounter.

The continuum measurements from 22 December 2003 also have relatively large uncertainties associated with them due mostly to the brightening twilight sky. While the largest aperture measurement yields an $A(\theta)f\rho$ value of 170 cm, in good agreement with our original prediction of about 200±80 cm, the three smaller aperture measurements yield significantly larger values near 450 cm. This difference with aperture size is in the direction expected for Wild 2 given its steeper than ρ^{-1} dust profiles but is larger than the departure from ρ^{-1} alone can explain. We attribute the remainder of the difference among the points to the large intrinsic uncertainties associated with each data point. An unweighted average of the four points gives $A(\theta)f\rho$ of 380 cm, again apparently larger than predicted. However, the phase angle on 22 December 2003 was 15°, as opposed to the post-perihelion 1997 value of of 35°–39°in the data used for the prediction. Using the phase function from comet Halley, we can correct the predicted $A(\theta)f\rho$ to what would be expected at 15°, increasing it by 55% to 310±120 cm. Therefore our measured $A(\theta)f\rho$ is consistent with, but on the high end of, the predicted value, again implying that comet Wild 2 was behaving as expected during the Stardust encounter.

5.3 CCD Images — January 2004

On 5 January 2004, less than 3 days after the Stardust flyby, we obtained CCD images with four filters (Kron-Cousins R, red continuum (7128 Å), blue continuum (4450 Å) and CN) . Observing conditions were poor, with the sky brightening during twilight, occasional thin cirrus, and effective seeing around 4 arcsec. The observing circumstances are shown in Table 1. Although Wild 2 was faint (about 13th magnitude), the background sky level could be directly determined by sampling the regions of the frame that were not contaminated by coma. To improve the comet's signal, we produced a composite image for each filter, after carefully aligning the optocenter of each frame. Unfortunately, even after combining the frames, the S/N was poor in the red continuum and CN images, and the comet was only barely detectable in the blue continuum.

As well as can be determined, the narrowband continuum images have essentially the same morphology as seen in the broadband images, so we adopt the R data as being representative of the dust environment on this date. The composite R image is shown in Fig. 9, along with the same image enhanced by dividing out a ρ^{-1} profile. The only feature seen is the dust tail, extending to the northwest. Although this tail mimics the appearance of a trailed star, we confirmed that it was visible in individual images and that no stars were in the vicinity. There is no sign of any jet structure, even though the sub-solar latitude is -33° and the secondary source should be in sunlight during part of the nucleus' rotational cycle.

The most noteworthy item in the January 2004 images involves the radial profiles of the coma. Fig. 10 shows the sunward and anti-sunward profiles for the 2004 data, as well as for our two 1997 observations that bracket the corresponding observation time. In 2004 the coma falls off as ρ^{-1} in the anti-solar direction, but in the sunward direction it falls off much more sharply, at nearly ρ^{-2}. (We note that this steep slope is qualitatively consistent with the aperture effect of $A(\theta)f\rho$ noted in the previous section.) We were concerned that this steep slope was an artifact that could result from several different causes: a star behind the nucleus, creating an artificially steep profile; removal of too much sky background; or a problem with the alignment of the different images. To evaluate whether this slope was real, we performed a number of tests. First, we aligned the individual images to the star background and produced a composite image of the untrailed star field, which shows no stars near the nucleus, eliminating that potential cause. Next, we removed different amounts of sky, computing the radial profiles in each case, to see if the unusual slope disappeared. Even when it was clear that too little sky was removed, the slope in the sunward direction still remained steeper than -1.5. Thus, even if our sky removal has problems—and there is no indication that this is true—the coma is still steeper than normal. Finally, we measured the radial profile in the coma of individual images to see if there were alignment problems or other issues introduced by combining multiple frames. Although the results were of lower S/N, they were consistent with the results obtained from the composite version. Thus we conclude that the dramatic falloff in the January data is real.

As can be seen by comparing the different curves in Fig. 10, the January 2004 coma has a much steeper slope than was observed on any other date except for the drop at the edge of the parabolic envelope from 9 July 1997 (discussed earlier). The difference between the July 1997 and January 2004 profiles is that the former has a slope of -1 out to $\sim 2\times10^4$ km, at which point it rapidly drops to the sky level, whereas the latter starts to depart from a -1 slope at the edge of the seeing disk and increases its slope with distance. The most obvious difference in the coma between these two observations is that the July 1997 image shows the secondary jet, while none is visible in the 2004 image. If we assume that the general behavior from 1997 to 2004 has not changed, then we can surmise that the jet emission falls off with the canonical -1 slope, while the coma has a much steeper falloff when the jet is off. The gradually changing slope seen in 2004 is indicative of phenomena studied by Jewitt and Meech (1987) and more extensively by Baum et al. (1992), who found that it was most likely the result of grains fading — changing either their size or albedo — as their distance from the nucleus increases. This indicates that there may have been a significant amount of evolution of the dust grains, as a function of cometocentric distance, during the time of the Stardust encounter. Ultimately, detailed analysis of the in situ data, measured as the spacecraft approached and receded from closest approach, may help in determining whether the physical sizes of the grains were changing or whether they were simply becoming darker with time. Indeed, the swarms of particles measured by the Dust Flux Monitor (Tuzzolino et al. 2004) suggest that fragmentation is occurring, though this phenomenon represents very large grains rather than the small grains (a few microns) that we observe.

6 Summary

In support of the Stardust mission, we obtained 13 nights of narrowband photometry and 11 nights of imaging of Wild 2 during the 1997 and 2003/04 apparitions, to supplement the 8 nights of photometry that we obtained during the 1978 and 1983/84 apparitions. The observations include photometry only 12 days prior to the Stardust encounter and images 3 days after. Results of our analyses are summarized here.

- On multiple apparitions, we derived production rates for up to five different gas species and $A(\theta)f\rho$ for multiple continuum bandpasses, as a function of heliocentric distance. We found that the OH, NH and dust production all exhibit significant seasonal effects, peaking 11–12 weeks before perihelion, while the CN, C_2 and C_3 show no obvious asymmetry with respect to perihelion, suggesting possible heterogeneities among different sources on the nucleus. The peak OH production is $\sim 1.1 \times 10^{28}$ molecules s^{-1}, which corresponds to an active area 6 km^2 (or less for a continuously active polar source). Our observations in December 2003 determined that the comet was behaving as predicted and should have had an OH production rate of $4(\pm1)\times10^{27}$ molecules s^{-1} at the time of the Stardust encounter.

- We measured the production rate ratios for various species and found that in the A'Hearn et al. (1995) taxonomic classification system, comet Wild 2 is depleted of carbon chain molecules. The depletion, as measured by the CN-to-C_2 production rate ratio, remains constant as a function of time and of heliocentric distance.

- The continuum is moderately reddened and shows no trends as a function of time or heliocentric distance, even though $A(\theta)f\rho$ has a large asymmetry. Ratios of continuum images obtained at different wavelengths show no spatial variations, indicating that the dust in the jets is the same color as the dust in the rest of the coma.

- The coma exhibited a number of features during the 1997 observations: a broad primary fan jet, a narrower secondary jet, a classical dust tail, an anti-tail and a parabolic sunward envelope.

- The two-jet configuration that we derived is completely self-consistent with all of our observations, explaining the seasonal effects, the pole orientation and the lack of lightcurve variations.

- The primary fan jet remained essentially unchanged on timescales of hours, days and months, and thus the source that produces it must be located within 15° of the spin axis. We used the observed position angles of the fan to derive the orientation of the rotation pole: α=281°±5° and δ=+13°±7° (J2000). With this solution we find that the primary jet was continuously active during the pre-perihelion time frame and turned off around perihelion, which explains the seasonal effects in OH, NH and dust production. The constancy of the jet on a wide range of timescales also suggests that the nucleus is in a state of simple rotation.

- We have little data showing the secondary jet, but we were able to use the times at which the jet is active to constrain the latitude of its source to between −37° and −62°.

- Lightcurve measurements of the inner coma in February and March 1997 show no variations, even over time spans as long as 8 hours, so we cannot determine the comet's rotation period. Lack of variation is likely due to the fact that the sub-solar point is at high latitude at this time, so the primary jet remains continuously active.

- We used the turning distance in a simple fountain model of the coma, along with the parabolic envelope seen in July 1997, to derive a dust velocity of 0.14 km s^{-1}, assuming spherical grains of a few microns in size.

- Radial profile measurements from 5 March and 9 July 1997 allow us to compare the two jets. In March the coma falls off with a slope of -1.33, whereas in July it has the canonical -1 slope. Extrapolating these slopes in to the optocenter shows a dust production of 23 kg s^{-1} in March and 9 kg s^{-1} in July (if all of the light comes from optically important spherical grains assumed to be a few microns across). In both cases the quiescent coma has the same slope as the jet, which indicates that most, if not all, of the dust is emitted in the jets, and some fraction diffuses out to form the rest of the coma. This is further supported by the lack of color differences between the jets and the rest of the coma. In January 2004, with no jet visible, the coma drops off with a slope of -2 in the sunward direction, suggesting that the grains are evolving in some manner as they move away from the nucleus.

- Given our pole solution and the estimated source locations, we know that the primary jet was inactive during the Stardust encounter, and the secondary source would have been rotating in and out of sunlight. Although we saw no sign of any jets in our January 2004 images, we do not have enough information to determine whether or not the jet was on or off during the Stardust close approach.

Appendix: IHW, AM and KW Filter Recalibrations

While developing the calibration procedures for the HB narrowband filters (Farnham et al. 2000; hereafter, Paper 1), we took the opportunity to perform a recalibration of older narrowband comet filters. This was done to correct problems that existed in earlier calibrations, as well as to create a set of procedures for reducing, in a consistent manner, data obtained with the different filter sets. We performed these recalibrations for three earlier filter sets, of which the International Halley Watch (IHW) filters (A'Hearn 1991) are the most notable. For completeness, we also recalibrated the first standardized filter set, described by A'Hearn et al. (1979) and A'Hearn and Millis (1980) (hereafter referred to as the AM filters) and the original filters used by A'Hearn and Cowan (1975) and A'Hearn et al. (1977) to observe comets Kohoutek and West (hereafter referred to as the KW filters). The recalibrations were performed using the same methodology set up for the HB filters; therefore we refer the reader to the detailed discussions in Farnham et al. (2000) for the basic procedures and will present here only the equations, coefficients and issues that deviate as a result of differences in the filter designs.

Improvements in the calibrations are primarily the result of three basic factors that are taken into account in the recalibration. First, we have access to better cometary spectra, with very little continuum underlying the gas bands. We can combine these high-quality spectra with each filter profile to determine what fraction of the desired emission band is being measured and to ultimately compute more accurate production rates. Second, the small amount of underlying continuum in the spectra reveals the extent of the wings of the C_2 and C_3 bands. This gives us a better understanding of contamination from these species, allowing us to more cleanly remove their effects from the dust and gas measurements. Finally, we have an improved method for computing the non-linear atmospheric extinction for the OH filters and can therefore obtain more accurate measurements of the OH flux. Other secondary factors, such as filter degradation with time, can also be addressed but are more difficult to correct and must be done on a case-by-case basis.

We first discuss the OH filters for the IHW and AM sets, with an emphasis on how they differ from the HB filters. Next, we present the equations needed for determining the extinction. Then we address the general reduction procedures and give the necessary equations for all of the filters in the IHW, AM and KW filter sets.

A.1. OH Extinction: IHW and AM Filters

As discussed in Paper 1, the OH extinction is difficult to compute because the ozone component changes dramatically across the filter bandpass, causing the extinction to be non-linear with respect to airmass. For the HB filter we found that we were able to produce reasonable models of the ozone and Rayleigh components of the extinction, and, by measuring the aerosol contribution with the BC filter, we could obtain a good match to the total observed extinction. We used this same approach for the IHW and AM filters, with minor modifications needed for the variations in the filter design. (There is no OH filter in the KW set, so it is not addressed.)

The IHW OH filter, like the HB filter, was designed to capture only the 0–0 OH band. Unfortunately, the IHW filter has a red leak at 3650 Å, with a transmission of about 0.2% (compared with 40% in the main bandpass), and difficulties arise because the red leak is not affected by the extreme ozone absorption. As the airmass increases, the main bandpass is rapidly extincted, and the relative contribution from the red leak becomes more prominent. At high airmass the signal from the red leak can even dominate over the signal from the main bandpass, giving a misleading OH measurement.

The AM OH filter, on the other hand, has no red leak but is very broad, with a width of 400 Å. Because of this width the AM filter captures both the 0–0 and 1–1 bands of OH, which must be taken into account when converting from fluxes to production rates. The width of the filter also affects the extinction in a non-linear manner, though it is somewhat cleaner than the IHW filter because it does not have a large moment arm that is produced by the IHW red leak.

For both of these filters the extinction is computed in the same manner as for the HB filters. We assembled polynomials with different coefficients for flux standards, solar analogs and comets with two different continuum levels (Tables A1 and A2). Coefficients for the different objects are necessary because of the difference in their spectral slopes and because of the presence of the OH band in the comet. These polynomials are used to find the extinction that best matches the standard star observations, and then the computed extinctions are applied to the comet measurements. Unfortunately, the IHW red leak and the broadness of the AM filter both introduce a significant amount of curvature into the extinction solutions, and this is reflected in more complicated polynomials than were seen for the HB filter.

In general, the same procedures and equations presented in Appendix A of Paper 1 are used to compute the extinction for both the IHW and AM OH measurements. However, there are two main differences. First, the number of terms in Eqs. 15–19 of Paper 1 need to be adjusted to account for the coefficients listed in Tables A1 and A2. Second, Eqs. 12 and 14 from Paper 1 are specific to the HB filter. For the IHW reductions these should be replaced with

$$E_{R_{\rm BC}} = 0.1780 \exp\left(-h/7.5\right) \tag{1}$$

and

$$E_{A_{\rm OH}} = (3077/4852)^{-0.8} E_{A_{\rm BC}}, \tag{2}$$

respectively.

For the AM filters, Eq. 12 from Paper 1 is replaced with

$$E_{R_{\rm GC}} = 0.1293 \exp\left(-h/7.5\right). \tag{3}$$

The location of the GC filter in the AM set introduces an additional problem that had to be addressed. This filter is centered at 5240 Å, which is in the wavelength region where the ozone extinction rises back up to a low, but non-negligible, level. Because we use the GC filter to compute the extinction from aerosols, we need to estimate the ozone contribution so it can be removed. To do this, we modeled the extinction at 5240 Å and found that ozone produced an average of 0.024 mag airmass^{-1} of extinction. We adopted this value for the ozone contribution in the GC filter and make the assumption that the rest of the GC extinction comes from aerosols. Thus Eq. 14 from Paper 1 is replaced with

$$E_{A_{\rm OH}} = (3137/5246)^{-0.8} (E_{A_{\rm GC}} - 0.024). \tag{4}$$

During our reanalysis of the IHW extinction we performed tests using several nights on which we had obtained data with both the HB and IHW filters. These tests, described fully in Paper 1, highlighted two issues that are relevant to the IHW reductions. First, as part of the OH extinction analysis, we solve for the thickness of the ozone, $t_{\rm oz}$, which determines the amount of ozone extinction in the UV. During our testing, we consistently found an offset of 0.02 cm in the ozone thicknesses as computed from the two filter sets. However, even though the computed thicknesses differ, the final results for the two OH filters tend to agree well. This indicates that the computed ozone thickness may be affected, in different ways for the different OH filters, by non-linearities in the ozone extinction (that are not accounted for in our polynomials). In other words, t_{oz} is not the true physical ozone thickness but may represent a scaled thickness that is used for computational purposes.

The second issue regarding the IHW filters also involves the ozone thickness but is relevant only in cases for which standard stars were measured at only two airmasses. In Paper 1 we describe how we start with a t_{oz}=0.15 and increase the thickness until the computed extinction matches the observations of the standard stars. Our analysis showed that one side effect of the IHW red leak was that the polynomials used to compute the ozone extinction produced highly curved solutions (due to the increasing influence of the red leak at large airmass). If only two airmass measurements were obtained, then two values of t_{oz} can reproduce equally well the extinction observed in the standard stars. If this is the case, the normal reduction procedure will always converge on the smallest thickness first, even though it is not always the correct one. To combat this problem, we must alter the procedures for cases in which only two airmass measurements were obtained. Thus we step through the ozone thickness twice, staring at 0.15 and working up, then starting at 0.45 and stepping down. If the solution converges on the same t_{oz} in each case, then that solution is the correct one. If different thicknesses are obtained in stepping up and stepping down, then other information (i.e., the offset in the instrumental magnitude zero point) must be used interactively to select the correct t_{oz}. We stress that if observations were obtained at three or more airmasses, then there is enough information to uniquely determine t_{oz} from stepping in one direction.

We have no AM filter data that was obtained simultaneously with a second filter set, so we could not perform tests intercomparing the results from the different filters. However, we did test the AM calibrations on data from well-studied comets, and the procedures appear to produce reasonable results. We note that t_{oz} is not well determined with this filter because the wide bandpass produces an extinction solution with a broad, shallow minimum. However, the extinction itself does appear to be determined accurately, with an uncertainty that is small in comparison with other factors such as the problems associated with dusty versus gassy comets. Thus, even though we cannot compare the results with other filters, we believe that our recalibration is a dramatic improvement over the original, and since the same procedures and models are being used, we should be getting consistent results for the OH filters in the HB, IHW and AM filter sets.

A.2. IHW Filters: General Reductions

The IHW filters are, for the most part, very similar to the HB filters. All of the gas (OH, NH, CN, C_3 and C_2) and ion (CO^+ and H_2O^+) species were designed to capture the same bands; however, the IHW filter profiles tend to have rounder profiles and slight offsets from the HB filters. These variations introduce slight changes in the signal measured through the filters, which means that the IHW reduction coefficients will be different from the HB coefficients, even though the reduction procedures are essentially identical. The most significant difference between the two filter sets is that the continuum bandpasses are located at different wavelengths. In the IHW set the UC filter is at 3365 Å, BC is at 4845 Å and RC is at 6840 Å. Shortly after the original IHW calibrations were completed, it became apparent that C_2 contamination of the BC bandpass was more severe than originally thought. Also, the UC bandpass was contaminated by the extended wing of the C_3 complex, and an NH_2 emission feature was located within the RC bandpass. Although we have no way to remove the RC contaminants, we can remove the UC and BC contaminants in the same manner as is done for the UC and GC filters in the HB set. Thus the basic reduction procedures for the IHW filters are identical to those for the HB filters, with one fewer continuum band that needs to be addressed. Because of the different wavelengths the coefficients in most of the equations will also change. Given here is a brief outline of the data reduction and equations. The interested reader is directed to Appendix D of Paper 1 for a complete discussion. These instructions represent updated calibration procedures for the IHW filters and supersede those outlined by A'Hearn (1991).

1. *Convert IHW magnitudes to fluxes in arbitrary (linearized) units.* Before this step the observed magnitudes should have been corrected to IHW magnitudes above the Earth's atmosphere (m_{XX}), as described in Paper 1. These magnitudes are then converted to linearized fluxes via the basic relation

$$f_{XX} = 10^{-0.4 m_{XX}}. \tag{5}$$

Ultimately, the linearized flux can be converted to an absolute flux using

$$F_{XX} = F_{0_{XX}} f_{XX}, \tag{6}$$

where $F_{0_{XX}}$ (listed in Table A3) is the absolute flux of a zero magnitude star in the XX filter. Note that in the equations below, f_{XX} denotes the linearized flux in species XX, while f'_{XX} denotes the flux from which continuum and/or contamination have been removed. Similarly, F and F' denote contaminated and decontaminated absolute fluxes, respectively.

As an aside, we note that the absolute flux calibration coefficients for the IHW filters were computed in the same manner as those for the HB filters; however we must highlight one important difference. The Hβ line at 4861 Å lies within the BC filter bandpass, which means that an interpolation of the flux between two points several hundred angstroms apart cannot be used to calibrate this filter. To account for the Hβ line, we were restricted to the use of spectrophotometric stars for which calibrated spectra exist. Thus, for the IHW BC filter calibration we used the stars listed by Hamuy et al. (1992) and unpublished spectra from A'Hearn (private communication). The result of this change is that the derived fluxes at 4845 Å decreased by about 10% from the original calibrations.

2. *Decontaminate the continuum measurements.* We assume that a measurement was obtained with the BC filter to provide a solid basis from which the continuum can be measured. If necessary, solar colors can be used to extrapolate from BC to other filters for removing the underlying continuum from the gas bands. On the other hand, if UC and/or RC observations were obtained, then they can be used to determine the color of the dust, which in turn allows for a more accurate removal of the underlying continuum. Unfortunately, both the BC and UC filters have small amounts of gas contamination. If a measurement was obtained with the C_2 filter, then the BC filter can be decontaminated. If not, then it must be assumed that all of the BC flux comes from continuum. Likewise, if a C_3 measurement was not obtained, then all of the UC flux must be assumed to come from continuum.

First, if neither UC nor RC were measured, then the BC filter is decontaminated by assuming solar colors for the dust:

$$f'_{\mathrm{BC}} = \frac{f_{\mathrm{BC}} - K_{\mathrm{BC1}} f_{\mathrm{C_2}}}{1 - K_{\mathrm{BC2}}}, \tag{7}$$

where the K coefficients are listed in Table A4. If both the UC and BC filters were measured, then they are decontaminated simultaneously by alternately iterating on the equations

$$f'_{\rm BC} = f_{\rm BC} - K_{\rm BC1} f_{\rm C_2} + K_{\rm BC3} (f'_{\rm UC})^{-0.247} (f'_{\rm BC})^{+1.247} \tag{8}$$

$$f'_{\rm UC} = f_{\rm UC} - K_{\rm UC1} f_{\rm C_3} + K_{\rm UC3} (f'_{\rm UC})^{+0.657} (f'_{\rm BC})^{+0.343}. \tag{9}$$

The final option is for cases in which both BC and RC were measured, and the color between these filters is used to decontaminate the BC measurement. Because there is no information about NH_2 that can be used for decontamination of the RC filter, it is assumed that

$$f'_{\rm RC} \equiv f_{\rm RC}. \tag{10}$$

Then the decontamination of BC is done by iterating on

$$f'_{\rm BC} = f_{\rm BC} - K_{\rm BC1} f_{\rm C_2} + K_{\rm BC4} (f'_{\rm BC})^{+0.852} (f'_{\rm RC})^{+0.148}. \tag{11}$$

3. *Compute the continuum colors.* Once all of the available continuum measurements have been decontaminated, the colors between these filters can be determined:

$$R_{\rm UC-BC} = 0.837 \left[2.5 \log \frac{f'_{\rm BC}}{f'_{\rm UC}} - (m_{\odot \rm UC} - m_{\odot \rm BC}) \right] \tag{12}$$

$$R_{\rm BC-RC} = 0.501 \left[2.5 \log \frac{f'_{\rm RC}}{f'_{\rm BC}} - (m_{\odot \rm BC} - m_{\odot \rm RC}) \right], \tag{13}$$

where the solar magnitudes are listed in Table A3. If a UC or RC measurement was not obtained, then the corresponding color can either be set to zero (solar colors), or it can be assigned the same color that is found from the other filters ($R_{\rm UC-BC} = R_{\rm BC-RC}$). If only BC was measured, then both colors are set to zero (solar colors) unless other information is available to constrain them.

4. *Compute the continuum underlying the gas and ion species.* The continuum flux, f'_{XX_C}, underlying the measurement of species XX is computed using

$$f'_{\rm OH_C} = f'_{\rm BC} 10^{-0.4(m_{\odot \rm OH} - m_{\odot \rm BC})} 10^{-0.704 R_{\rm UC-BC}} \tag{14}$$

$$f'_{\rm NH_C} = f'_{\rm BC} 10^{-0.4(m_{\odot \rm NH} - m_{\odot \rm BC})} 10^{-0.585 R_{\rm UC-BC}} \tag{15}$$

$$f'_{\rm CN_C} = f'_{\rm BC} 10^{-0.4(m_{\odot \rm CN} - m_{\odot \rm BC})} 10^{-0.389 R_{\rm UC-BC}} \tag{16}$$

$$f'_{\rm C_{3C}} = f'_{\rm BC} 10^{-0.4(m_{\odot \rm C3} - m_{\odot \rm BC})} 10^{-0.314 R_{\rm UC-BC}} \tag{17}$$

$$f'_{\rm CO^+{}_C} = f'_{\rm BC} 10^{-0.4(m_{\odot \rm CO^+} - m_{\odot \rm BC})} 10^{-0.234 R_{\rm UC-BC}} \tag{18}$$

$$f'_{\rm C_{2C}} = f'_{\rm BC} 10^{-0.4(m_{\odot \rm C2} - m_{\odot \rm BC})} 10^{+0.120 R_{\rm BC-RC}} \tag{19}$$

$$f'_{\rm H_2O^+{}_C} = f'_{\rm BC} 10^{-0.4(m_{\odot \rm H_2O^+} - m_{\odot \rm BC})} 10^{+0.870 R_{\rm BC-RC}} \tag{20}$$

5. *Convert all fluxes to absolute values.* In order to remove the continuum contribution from the gas and ion measurements, the fluxes all need to be converted to absolute values. This is done with equation 6 above, in the manner described in Paper 1.

At this point, $Af\rho$ values (in cm) can also be computed for each of the continuum filters, as described in Paper 1. The relevant coefficients are $q_{\rm UC} = 2.219 \times 10^{17}$, $q_{\rm BC} = 1.292 \times 10^{17}$ and $q_{\rm RC} = 1.770 \times 10^{17}$.

6. *Remove continuum and contamination and convert to full band fluxes.* This step, including the equations, is identical to that for the HB filters and is described in Paper 1. The relevant IHW coefficients are listed in Table A3.

A.3. AM Filters: General Reductions

This filter set was designed to measure only the five gas species with no ions. Originally, there were four continuum filters (3300, 3675, 3930 and 5240 Å), with one situated next to each gas band. However, it became clear that the 3300 Å bandpass had too low a signal, and the 3930 Å bandpass was so badly contaminated that they were worthless for determining the background continuum level. Therefore only the 3675 Å (UC) and the 5240 Å (GC) bands, which are only slightly contaminated by C_3 and C_2, respectively, are utilized here.

The AM filters are again similar in design to the HB filters, allowing the same procedures to be used. Thus the step numbers given below refer to the steps listed in the IHW procedures above and to the steps in Paper 1.

1. The AM magnitudes, corrected to above the atmosphere, are converted to linearized fluxes using Eqs. 5 and 6, where the necessary absolute flux conversions are given in Table A5.

2. We assume that an observation was made with the GC filter to provide a high signal measurement of the continuum. If an observation was also made with the UC filter, then we can determine the color of the continuum. As before, we must have a C_2 measurement to decontaminate the GC filter and a C_3 measurement to decontaminate the UC filter. If the gas species were not measured, the flux must be assumed to come entirely from continuum.

If just the GC filter was used, then we assume solar colors to remove the C_2 contamination:

$$f'_{\rm GC} = \frac{f_{\rm GC} - K_{\rm GC1} f_{\rm C_2}}{1 - K_{\rm GC2}}, \tag{21}$$

where the coefficients are listed in Table A6. If both the UC and GC filters were used, then they are decontaminated by iterating on

$$f'_{\rm GC} = f_{\rm GC} - K_{\rm GC1} f_{\rm C_2} + K_{\rm GC3} (f'_{\rm UC})^{+0.067} (f'_{\rm GC})^{+0.933} \tag{22}$$

$$f'_{\rm UC} = f_{\rm UC} - K_{\rm UC1} f_{\rm C_3} + K_{\rm UC3} (f'_{\rm UC})^{+0.764} (f'_{\rm GC})^{+0.236}. \tag{23}$$

until they converge.

3. If both UC and GC were measured, then the continuum colors are determined from

$$R_{\rm UC-GC} = 0.639 \left[2.5 \log \frac{f'_{\rm GC}}{f'_{\rm UC}} - (m_{\odot \rm UC} - m_{\odot \rm GC}) \right], \tag{24}$$

where the solar magnitudes are listed in Table A5. If the UC filter was not measured, then the continuum color is set to zero (solar colors).

4. The continua underlying the gas species are computed from

$$f'_{\rm OH_C} = f'_{\rm GC} 10^{-0.4(m_{\odot \rm OH} - m_{\odot \rm GC})} 10^{-0.844 R_{\rm UC-GC}} \tag{25}$$

$$f'_{\rm NH_C} = f'_{\rm GC} 10^{-0.4(m_{\odot \rm NH} - m_{\odot \rm GC})} 10^{-0.742 R_{\rm UC-GC}} \tag{26}$$

$$f'_{\rm CN_C} = f'_{\rm GC} 10^{-0.4(m_{\odot \rm CN} - m_{\odot \rm GC})} 10^{-0.550 R_{\rm UC-GC}} \tag{27}$$

$$f'_{\rm C_{3_C}} = f'_{\rm GC} 10^{-0.4(m_{\odot \rm C3} - m_{\odot \rm GC})} 10^{-0.478 R_{\rm UC-GC}} \tag{28}$$

$$f'_{\rm C_{2_C}} = f'_{\rm GC} 10^{-0.4(m_{\odot \rm C2} - m_{\odot \rm GC})} 10^{-0.464 R_{\rm UC-GC}}. \tag{29}$$

5. The fluxes are converted to absolute values using Eq. 6. Also, the $Af\rho$ values can be computed with the coefficients, $q_{\rm UC} = 2.090 \times 10^{17}$, $q_{\rm GC} = 1.335 \times 10^{17}$.

6. Again, this step is identical to that given in Paper 1, with the AM coefficients listed in Table A5.

A.4. KW Filters: General Reductions

This last filter set consists of only the CN, C_3, BC (4527 Å) and C_2 filters. Originally there was a UC filter at 3915 Å, but, like the AM 3930 Å filter, it is too badly contaminated to be of use. Thus we have only one continuum filter available and so must assume solar colors for all extrapolations to other wavelengths. The BC filter is contaminated by C_2 and the CN filter is contaminated by C_3, both of which can be removed during the reductions.

The reduction procedures for the KW filters follow a somewhat abbreviated form of the HB reductions. These changes are mainly caused by two factors: First, there are fewer filters, forcing a more straightforward set of reduction steps; and second, no magnitude system was set up for this filter set. Instead, the data obtained with these filters were converted to flux units, F_{XX}, using the standard star Regulus. Thus all of our reductions must be performed using these fluxes.

Decontaminating the BC filter is done using the relation

$$F'_{\mathrm{BC}} = \frac{F_{\mathrm{BC}} - K_{\mathrm{BC1}} F_{\mathrm{C_2}}}{1 - K_{\mathrm{BC1}}(F_{\odot_{\mathrm{C_2}}}/F_{\odot_{\mathrm{BC}}})}, \tag{30}$$

where the solar flux coefficients are listed in Table A7 and $K_{\mathrm{BC1}} = 0.1378$. Next, we compute the continuum under the gas bands,

$$F'_{\mathrm{CN}_C} = F'_{\mathrm{BC}}(F_{\odot_{\mathrm{CN}}}/F_{\odot_{\mathrm{BC}}}) \tag{31}$$

$$F'_{\mathrm{C_2}C} = F'_{\mathrm{BC}}(F_{\odot_{\mathrm{C_2}}}/F_{\odot_{\mathrm{BC}}}) \tag{32}$$

$$F'_{\mathrm{C_3}C} = F'_{\mathrm{BC}}(F_{\odot_{\mathrm{C_3}}}/F_{\odot_{\mathrm{BC}}}). \tag{33}$$

The continuum and contamination are removed from the gas fluxes using Eqs. 46, 47 and 49 from Paper 1, with the KW coefficients listed in Table A7 and $\gamma_{\mathrm{CN/C_3}} = 1.41 \times 10^{-3}$. Finally, $Af\rho$ for the BC filter is computed using the coefficient $q_{\mathrm{BC}} = 1.234 \times 10^{17}$.

Acknowledgements

We would like to thank R. Millis and M. A'Hearn for the acquisition of observations and D. Osip for preliminary reductions and analyses of the data from the first two apparitions of comet Wild 2. We also thank S. Lederer and D. Osip for obtaining images on 1 and 5 March 1997.

Image processing in this paper has been performed using the IRAF program. IRAF is distributed by the National Optical Astronomy Observatories, which is operated by the Association of Universities for Research in Astronomy, Inc. (AURA) under cooperative agreement with the National Science Foundation.

This research was funded, in part, by NASA grants NAG5-12509 and NAG5-13379 and their predecessors.

References

A'Hearn, M. F. 1991. Photometry and Polarimetry Network. In: Sekanina, Z. (Ed.), The Comet Halley Archive Summary Volume. Jet Propulsion Laboratory, Pasadena, pp. 193–235.

A'Hearn, M. F., Cowan, J. J. 1975. Molecular production rates in Comet Kohoutek. Astron. J. 80, 852–860.

A'Hearn, M. F., Millis, R. L. 1980. Abundance correlations among comets. Astron. J. 85, 1528–1537.

A'Hearn, M. F., Millis, R. L., Birch, P. V. 1979. Gas and dust in some recent periodic comets. Astron. J. 84, 570–579.

A'Hearn, M. F., Millis, R. L., Schleicher, D. G., Osip, D. J., Birch, P. V. 1995. The ensemble properties of comets: Results from narrowband photometry of 85 comets, 1976-1992. Icarus 118, 223–270.

A'Hearn, M. F., Schleicher, D. G., Millis, R. L., Feldman, P. D., Thompson, D. T. 1984. Comet Bowell 1980b. Astron. J. 89, 579–591.

A'Hearn, M. F., Thurber, C. H., Millis, R. L. 1977. Evaporation of ices from Comet West. Astron. J. 82, 518–524.

Baum, W. A., Kreidl, T. J., Schleicher, D. G. 1992. Cometary grains. Astron. J. 104, 1216–1225.

Brownlee, D. E., Horz, F., Newburn, R. L., Zolensky, M., Duxbury, T. C., Sandford, S., Sekanina, Z., Tsou, P., Hanner, M. S., Clark, B. C., Green, S. F., Kissel, J. 2004. Surface of young Jupiter family comet 81P/Wild 2: View from the Stardust spacecraft. Science 304, 1764–1769.

Cochran, A. L., Green, J. R., Barker, E. S. 1989. Are low-activity comets intrinsically different from more active comets? Icarus 79, 125–144.

Cochran, A. L., Schleicher, D. G. 1993. Observational constraints on the lifetime of cometary H_2O. Icarus 105, 235–253.

Cowan, J. J., A'Hearn, M. F. 1979. Vaporization of comet nuclei - Light curves and life times. Moon and Planets 21, 155–171.

Crovisier, J., Colom, P., Gérard, E., Bockelée-Morvan, D., Bourgois, G. 2002. Observations at Nançay of the OH 18-cm lines in comets. The data base. Observations made from 1982 to 1999. Astron. Astrophys. 393, 1053–1064.

Devine, N. 1981. A simple radiation model of cometary dust for P/Halley. In: SP-174, pp. 47–53.

Farnham, T. L. 2001. The rotation axis of the centaur 5145 Pholus. Icarus 152, 238–245.

Farnham, T. L., Cochran, A. L. 2002. A McDonald Observatory study of comet 19P/Borrelly: Placing the Deep Space 1 observations into a broader context. Icarus 160, 398–418.

Farnham, T. L., Davies, J. K. 2003. The rotational and physical properties of the Centaur (32532) 2001 PT_{13}. Icarus 164, 418–427.

Farnham, T. L., Schleicher, D. G., A'Hearn, M. F. 2000. The HB narrowband comet filters: standard stars and calibrations. Icarus 147, 180–204.

Fink, U., Hicks, M. P., Fevig, R. A. 1999. Production Rates for the Stardust Mission Target: 81P/Wild 2. Icarus 141, 331–340.

Grün, E., Jessberger, E. K. 1990. Dust. In: Huebner, W. F. (Ed.), Physics and Chemistry of Comets. Springer-Verlag, New York, pp. 113–176.

Hamuy, M., Walker, A., Suntzeff, N., Gigoux, P., Heathcote, S., Phillips, M. 1992. Southern spectrophotometric standards. I. . Publ. Astron. Soc. Pacific 104, 533–552.

Hanner, M. S., Hayward, T. L. 2003. Infrared observations of Comet 81P/Wild 2 in 1997. Icarus 161, 164–173.

Jewitt, D. C., Meech, K. J. 1987. Surface brightness profiles of 10 comets. Astrophys. J. 317, 992–1001.

Landolt, A. 1992. UBVRI photometric standard stars in the magnitude range 11.5-16.0 around the celestial equator. Astron. J. 104, 340–371.

Mäkinen, J. T. T., Silén, J., Schmidt, W., Kyrölä, E., Summanen, T., Bertaux, J.-L., Quémerais, E., Lallement, R. 2001. Water production of comets 2P/Encke and 81P/Wild 2 derived from SWAN observations during the 1997 apparition. Icarus 152, 268–274.

Newburn, R., Acton, C., Bhaskaran, S., Brownlee, D., Cheuvront, A., Duxbury, T., Hanner, M., Semenov, B., Sandford, S., Tsou, P. 2004. Stardust Imaging of Comet Wild 2: First Look. In: Lunar and Planetary Institute Conference Abstracts, Volume XXXV, pp. 1437.

Osip, D. J., Schleicher, D. G., Millis, R. L. 1992. Comets - Groundbased observations of spacecraft mission candidates. Icarus 98, 115–124.

Pittichová, J., Meech, K. J. 2001. Rotation of Comet 81P/Wild 2. Bull. Am. Ast. Soc. 33, 1075.

Sanzovo, G. C., de Almeida, A. A., Misra, A., Torres, R. M., Boice, D. C., Huebner, W. F. 2001. Mass-loss rates, dust particle sizes, nuclear active areas and minimum nuclear radii of target comets for missions STARDUST and CONTOUR. Mon. Not. R. Astron. Soc. 326, 852–868.

Schleicher, D. G., Millis, R. L., Birch, P. V. 1998. Narrowband Photometry of Comet P/Halley: Variation with Heliocentric Distance, Season, and Solar Phase Angle. Icarus 132, 397–417.

Schleicher, D. G., Osip, D. J. 2002. Long- and Short-Term Photometric Behavior of Comet Hyakutake (1996 B2). Icarus 159, 210–233.

Schleicher, D. G., Woodney, L. M., Millis, R. L. 2003. Comet 19P/Borrelly at multiple apparitions: seasonal variations in gas production and dust morphology. Icarus 162, 415–442.

Schulz, R., Stüwe, J. A., Boehnhardt, H., Gaessler, W., Tozzi, G. P. 2003. Characterization of STARDUST target comet 81P/Wild 2 from 1996 to 1998. Astron. Astrophys. 398, 345–352.

Sekanina, Z. 2003. A model for comet 81P/Wild 2. J. Geophys. Res. (Planets) 108 (E10), 8112.

Sekanina, Z., Brownlee, D. E., Economou, T. E., Tuzzolino, A. J., Green, S. F. 2004. Modeling the nucleus and jets of comet 81P/Wild 2 based on the Stardust encounter data. Science 304, 1769–1774.

Tuzzolino, A. J., Economou, T. E., Clark, B. C., Tsou, P., Brownlee, D. E., Green, S. F., McDonnell, J. A. M., McBride, N., Colwell, T. S. H. 2004. Dust measurements in the coma of comet 81P/Wild 2 by the dust flux monitor instrument. Science 304, 1776–1780.

TABLE 1

Observing Circumstances and Fluorescence Efficiencies for Comet 81P/Wild 2

	ΔT	r_H	Δ	Phase	PA of	$\dot{r}_H$	log L/N^a (erg s^{-1} molecule^{-1})			
UT Date	(day)	(AU)	(AU)	Angle (°)	Sun (°)	(km s^{-1})	OH	NH	CN	Inst
1978 Mar 8.17	−99.71	1.803	1.388	33.1	NA	−9.3	−14.629	−13.147	−12.460	Phot
1978 Jun 3.20	−12.68	1.497	1.726	35.8	NA	−1.6	−14.754	−13.211	−12.554	Phot
1978 Jun 5.18	−10.70	1.495	1.733	35.7	NA	−1.4	−14.760	−13.218	−12.563	Phot
1978 Jun 8.19	−7.69	1.493	1.745	35.5	NA	−1.0	−14.771	−13.232	−12.579	Phot
1983 Dec 30.32	−233.85	2.621	1.762	12.8	NA	−10.6	−14.524	−13.179	−12.519	Phot
1984 Jan 31.22	−201.95	2.423	1.913	22.6	NA	−10.8	−14.514	−13.184	−12.518	Phot
1984 Feb 1.25	−200.92	2.417	1.919	22.8	NA	−10.8	−14.514	−13.184	−12.518	Phot
1984 Feb 27.20	−174.97	2.254	2.095	26.0	NA	−10.8	−14.514	−13.184	−12.513	Phot
1997 Jan 17.38	−109.25	1.906	0.924	2.1	NA	−8.8	−14.717	−13.137	−12.454	Phot
1997 Jan 19.50	−107.13	1.895	0.912	1.1	NA	−8.7	−14.725	−13.135	−12.451	Phot
1997 Feb 1.52	−94.11	1.832	0.862	8.1	276.6	NA	NA	NA	NA	CCD
1997 Feb 3.50	−92.13	1.823	0.858	9.4	NA	−8.0	−14.770	−13.125	−12.436	Phot
1997 Feb 12.26	−83.37	1.783	0.850	15.0	NA	−7.6	−14.782	−13.121	−12.431	Phot
1997 Feb 14.29	−81.34	1.774	0.850	16.3	279.6	NA	NA	NA	NA	CCD
1997 Feb 15.17	−80.46	1.770	0.850	16.8	NA	−7.4	−14.785	−13.120	−12.429	Phot
1997 Mar 1.18	−66.45	1.714	0.871	24.5	280.6	NA	NA	NA	NA	CCD
1997 Mar 5.27	−62.36	1.700	0.881	26.5	280.9	NA	NA	NA	NA	CCD
1997 Mar 5.39	−62.24	1.699	0.882	26.5	NA	−6.1	−14.771	−13.122	−12.431	Phot
1997 Mar 16.43	−51.20	1.664	0.919	30.9	281.7	NA	NA	NA	NA	CCD
1997 Mar 31.19	−36.44	1.624	0.983	35.3	283.2	NA	NA	NA	NA	CCD
1997 Apr 25.21	−11.42	1.587	1.114	39.0	286.7	NA	NA	NA	NA	CCD
1997 May 1.22	−5.41	1.584	1.150	39.4	NA	−0.6	−14.821	−13.246	−12.588	Phot
1997 Jun 4.22	+28.59	1.608	1.382	38.7	NA	+3.1	−14.682	−13.310	−12.430	Phot
1997 Jun 5.19	+29.56	1.610	1.389	38.7	NA	+3.2	−14.676	−13.309	−12.424	Phot
1997 Jul 1.21	+55.58	1.677	1.615	35.9	NA	+5.6	−14.578	−13.260	−12.344	Phot
1997 Jul 2.20	+56.57	1.680	1.625	35.8	NA	+5.7	−14.576	−13.259	−12.343	Phot
1997 Jul 3.19	+57.56	1.683	1.634	35.7	NA	+5.8	−14.574	−13.257	−12.342	Phot
1997 Jul 9.19	+63.56	1.704	1.693	34.8	292.5	NA	NA	NA	NA	CCD
1997 Sep 30.10	+146.47	2.108	2.699	19.5	282.6	NA	NA	NA	NA	CCD
1997 Oct 1.10	+147.47	2.114	2.712	19.3	282.4	NA	NA	NA	NA	CCD
2003 Dec 22.56	+87.62	1.807	2.610	15.0	NA	+7.7	−14.567	−13.229	−12.338	Phot
2004 Jan 5.55	+101.61	1.873	2.602	17.2	101.4	NA	NA	NA	NA	CCD

[a] Fluorescence efficiencies are for $r_H = 1$ AU, and are scaled by r_H^{-2} in the reductions.

TABLE 2

Photometric Fluxes and Column Abundances for Comet 81P/Wild 2

UT Date	F^a	Aperture Size (arcsec)	Aperture log ρ (km)	log Emission Band Flux ($erg\ cm^{-2}\ s^{-1}$) OH	NH	CN	C_3	C_2	log Continuum Flux ($erg\ cm^{-2}\ s^{-1}\ Å^{-1}$) UV	Blue	Green	log M(ρ) (molecule) OH	NH	CN	C_3	C_2
1978 Mar 8.14	A	26.5	4.13	—	—	−11.75	—	−12.45	—	—	−13.73	—	—	28.95	—	28.14
1978 Mar 8.16	A	26.5	4.13	—	—	−11.80	—	−12.30	—	—	−13.78	—	—	28.91	—	28.29
1978 Mar 8.19	A	26.5	4.13	—	—	−11.70	—	—	—	—	−13.73	—	—	29.01	—	—
1978 Jun 3.19	A	109.7	4.84	—	—	−10.43	−10.90	−10.62	—	—	−13.11	—	—	30.40	29.38	30.00
1978 Jun 3.21	A	109.7	4.84	—	—	−10.45	−10.85	−10.63	—	—	−13.07	—	—	30.38	29.43	29.99
1978 Jun 5.17	A	55.1	4.54	—	—	−10.79	−11.23	−11.03	—	—	−13.36	—	—	30.05	29.04	29.59
1978 Jun 5.19	A	77.9	4.69	—	—	−10.61	−11.05	−10.80	—	—	−13.32	—	—	30.23	29.23	29.83
1978 Jun 8.18	A	38.7	4.39	—	—	−11.12	−11.41	−11.29	—	—	−13.37	—	—	29.74	28.87	29.34
1978 Jun 8.19	A	77.9	4.69	—	—	−10.61	−10.92	−10.75	—	—	−13.19	—	—	30.25	29.36	29.88
1978 Jun 8.21	A	77.9	4.69	—	—	−10.60	−11.04	−10.74	—	—	−13.18	—	—	30.26	29.24	29.88
1983 Dec 30.32	I	27.6	4.25	—	—	−12.68	—	−13.06	−14.73	—	−14.48	—	—	28.61	—	28.07
1984 Jan 31.22	I	38.9	4.43	−11.71	−12.83	−12.25	−12.24	—	−14.85	—	−14.27	31.58	29.14	29.04	28.55	—
1984 Feb 1.25	I	38.9	4.43	−11.64	−13.11	−12.25	−12.10	−12.84	−15.01	—	−14.46	31.66	28.86	29.04	28.68	28.28
1984 Feb 27.20	I	27.6	4.32	−11.77	−14.29	−12.33	−12.73	−12.82	−14.77	—	−14.43	31.54	27.69	28.98	28.07	28.32
1997 Jan 17.32	H	75.3	4.40	—	—	−11.23	−11.37	−11.56	—	−13.12	−13.07	—	—	29.17	28.57	28.73
1997 Jan 17.32	I	75.3	4.40	−11.06	−12.13	−11.19	−11.21	−11.64	−13.40	—	−12.98	31.60	28.95	29.20	28.73	28.65
1997 Jan 17.43	H	75.3	4.40	—	—	−11.28	−11.34	−11.55	—	−13.10	−13.08	—	—	29.12	28.61	28.74
1997 Jan 17.43	I	75.3	4.40	−11.09	−12.33	−11.23	−11.39	−11.94	−13.49	—	−13.01	31.57	28.75	29.17	28.55	28.35
1997 Jan 19.50	H	52.8	4.24	—	—	−11.52	−11.41	−11.85	—	−13.16	−13.10	—	—	28.86	28.52	28.42
1997 Jan 19.50	I	52.8	4.24	−11.27	−12.17	−11.48	−11.35	—	−13.57	—	−13.11	31.38	28.89	28.90	28.57	—
1997 Feb 3.50	H	55.1	4.23	—	—	−11.35	−11.36	−12.04	—	−13.10	−13.08	—	—	28.92	28.48	28.15
1997 Feb 3.50	I	55.1	4.23	−11.25	—	−11.26	−11.39	−12.35	−13.54	—	−13.06	31.36	—	29.02	28.45	27.83
1997 Feb 12.17	H	75.3	4.37	−10.81	−11.67	−10.91	−11.07	−11.28	−13.44	−13.04	−13.00	31.78	29.26	29.33	28.74	28.87
1997 Feb 12.17	I	75.3	4.37	−10.79	−11.68	−10.88	−10.94	−11.42	−13.47	—	−12.95	31.80	29.25	29.36	28.87	28.74
1997 Feb 12.26	H	37.5	4.06	—	—	−11.42	−11.47	−11.78	—	−13.26	−13.23	—	—	28.82	28.34	28.38
1997 Feb 15.17	H	37.5	4.06	−11.18	−12.09	−11.39	−11.38	−11.87	−13.71	−13.25	−13.22	31.41	28.83	28.85	28.42	28.28
1997 Feb 15.17	I	37.5	4.06	−11.14	−12.00	−11.39	−11.36	−11.85	−13.65	—	−13.19	31.44	28.92	28.84	28.44	28.30
1997 Mar 5.39	H	38.7	4.09	−10.99	—	−11.28	−11.30	−11.75	−13.81	−13.36	−13.29	31.58	—	28.95	28.50	28.40
1997 Mar 5.39	I	38.7	4.09	−11.21	−12.06	−11.30	−11.20	−11.82	−13.84	—	−13.26	31.36	28.86	28.93	28.60	28.33
1997 May 1.21	I	27.5	4.06	−11.46	−12.15	−11.76	−11.58	−11.86	−14.74	—	−14.02	31.33	29.06	28.80	28.39	28.45
1997 May 1.24	H	38.7	4.21	−11.23	—	−11.38	−11.36	−11.58	−13.95	−13.51	−13.51	31.56	—	29.17	28.61	28.74
1997 May 1.24	I	38.7	4.21	−11.37	−11.95	−11.35	−11.38	−11.74	−14.35	—	−13.67	31.42	29.27	29.21	28.59	28.58
1997 Jun 4.21	I	106.4	4.73	−10.57	−11.91	−10.69	−11.30	−11.09	−13.85	—	−13.34	32.25	29.54	29.88	28.84	29.40
1997 Jun 4.23	I	106.4	4.73	−10.56	−11.75	−10.72	−10.93	−11.33	−14.35	—	−13.33	32.26	29.71	29.85	29.21	29.16
1997 Jun 5.19	I	106.4	4.73	−10.51	−11.56	−10.65	−11.17	−11.01	−13.69	—	−13.36	32.32	29.90	29.92	28.97	29.48
1997 Jul 1.21	I	77.9	4.66	−10.87	−11.93	−10.85	−11.30	−11.37	−14.26	—	−13.56	32.02	29.64	29.80	29.01	29.29
1997 Jul 2.20	H	77.9	4.66	−10.71	—	−10.90	−11.33	−11.37	−13.94	−13.65	−13.54	32.18	—	29.76	28.99	29.30
1997 Jul 2.20	I	77.9	4.66	−10.82	−12.00	−10.85	−11.45	−11.34	−13.99	—	−13.55	32.08	29.58	29.81	28.87	29.32
1997 Jul 3.19	H	77.9	4.66	−10.77	−11.79	−10.94	−11.45	−11.33	−13.94	−13.64	−13.60	32.13	29.80	29.73	28.88	29.34
1997 Jul 3.19	I	77.9	4.66	−10.97	—	−10.90	—	−11.42	−13.84	—	−13.53	31.93	—	29.77	—	29.26
2003 Dec 22.55	H	60.7	4.76	—	—	−11.34	—	−11.86	—	—	−14.05	—	—	29.79	—	29.28
2003 Dec 22.55	H	37.5	4.55	—	—	−11.92	—	—	—	−13.81	−13.84	—	—	29.22	—	—
2003 Dec 22.56	H	23.9	4.35	—	—	—	—	—	—	−13.97	—	—	—	—	—	—

[a]Filter set: A = A'Hearn and Millis; I = IHW; H = HB (see text and Appendix for details).

TABLE 3

Photometric Production Rates for Comet 81P/Wild 2

UT Date	ΔT (day)	log r_H (AU)	F[a]	log ρ (km)	log Q^b (molecule s^{-1}) OH	NH	CN	C_3	C_2	log $A(\theta)f\rho^b$ (cm) UV	Blue	Green	log Q H_2O
1978 Mar 8.14	−99.74	0.256	A	4.13	—	—	25.21 .05	—	24.60 .09	—	—	2.62 .02	—
1978 Mar 8.16	−99.72	0.256	A	4.13	—	—	25.17 .06	—	24.76 .06	—	—	2.58 .02	—
1978 Mar 8.19	−99.69	0.256	A	4.13	—	—	25.27 .05	—	—	—	—	2.62 .02	—
1978 Jun 3.19	−12.69	0.175	A	4.84	—	—	25.58 .02	24.73 .04	25.36 .02	—	—	2.56 .02	—
1978 Jun 3.21	−12.67	0.175	A	4.84	—	—	25.55 .02	24.77 .04	25.36 .02	—	—	2.60 .02	—
1978 Jun 5.17	−10.71	0.175	A	4.54	—	—	25.60 .02	24.58 .04	25.34 .02	—	—	2.61 .02	—
1978 Jun 5.19	−10.69	0.175	A	4.69	—	—	25.58 .02	24.66 .04	25.37 .02	—	—	2.50 .02	—
1978 Jun 8.18	−7.70	0.174	A	4.39	—	—	25.50 .04	24.53 .07	25.29 .04	—	—	2.76 .02	—
1978 Jun 8.19	−7.69	0.174	A	4.69	—	—	25.60 .02	24.78 .05	25.42 .02	—	—	2.64 .02	—
1978 Jun 8.21	−7.67	0.174	A	4.69	—	—	25.61 .02	24.67 .07	25.42 .02	—	—	2.65 .02	—
1983 Dec 30.32	−233.85	0.418	I	4.25	—	—	24.89 .07	—	24.55 .35	2.26 .22	—	2.27 .04	—
1984 Jan 31.22	−201.95	0.384	I	4.43	27.70 .15	25.51 .24	24.97 .05	24.19 .20	—	1.96 .20	—	2.30 .04	27.65
1984 Feb 1.25	−200.92	0.383	I	4.43	27.77 .16	25.22 .35	24.97 .06	24.33 .16	24.41 .36	1.80 .25	—	2.11 .07	27.72
1984 Feb 27.20	−174.97	0.353	I	4.32	27.80 .14	24.20 .99	25.05 .05	23.84 .39	24.59 .25	2.16 .17	—	2.27 .05	27.76
1997 Jan 17.32	−109.31	0.280	H	4.40	—	—	25.02 .01	24.22 .03	24.78 .04	—	2.64 .01	2.70 .01	—
1997 Jan 17.32	−109.31	0.280	I	4.40	27.63 .02	25.22 .13	25.05 .01	24.37 .07	24.70 .08	2.60 .03	—	2.78 .01	27.63
1997 Jan 17.43	−109.20	0.280	H	4.40	—	—	24.97 .01	24.25 .03	24.79 .05	—	2.65 .01	2.69 .01	—
1997 Jan 17.43	−109.20	0.280	I	4.40	27.60 .04	25.03 .19	25.02 .02	24.20 .11	24.40 .16	2.51 .04	—	2.75 .01	27.60
1997 Jan 19.50	−107.13	0.278	H	4.24	—	—	24.96 .01	24.34 .03	24.72 .07	—	2.74 .01	2.82 .01	—
1997 Jan 19.50	−107.13	0.278	I	4.24	27.68 .05	25.43 .21	25.00 .03	24.40 .10	—	2.57 .05	—	2.79 .01	27.67
1997 Feb 3.50	−92.13	0.261	H	4.23	—	—	25.02 .02	24.31 .06	24.44 .19	—	2.72 .02	2.76 .02	—
1997 Feb 3.50	−92.13	0.261	I	4.23	27.64 .24	— .47	25.11 .04	24.28 .24	24.13 .55	2.52 .11	—	2.76 .01	27.64
1997 Feb 12.17	−83.46	0.251	H	4.37	27.84 .01	25.55 .02	25.20 .01	24.42 .02	24.95 .02	2.54 .02	2.62 .01	2.68 .01	27.85
1997 Feb 12.17	−83.46	0.251	I	4.37	27.86 .01	25.54 .04	25.24 .01	24.55 .03	24.81 .04	2.43 .03	—	2.72 .01	27.87
1997 Feb 12.26	−83.37	0.251	H	4.06	—	—	25.18 .01	24.39 .02	24.94 .05	—	2.70 .01	2.76 .01	—
1997 Feb 15.17	−80.46	0.248	H	4.06	27.96 .02	25.64 .06	25.20 .01	24.46 .05	24.84 .06	2.58 .04	2.71 .01	2.76 .01	27.97
1997 Feb 15.17	−80.46	0.248	I	4.06	28.00 .03	25.72 .08	25.19 .02	24.48 .07	24.85 .10	2.55 .04	—	2.77 .01	28.01
1997 Mar 5.39	−62.24	0.230	H	4.09	28.06 .09	—	25.23 .02	24.49 .08	24.88 .07	2.44 .09	2.56 .02	2.66 .02	28.08
1997 Mar 5.39	−62.24	0.230	I	4.09	27.84 .17	25.59 .18	25.22 .04	24.59 .11	24.81 .18	2.33 .11	—	2.67 .02	27.86
1997 May 1.21	−5.42	0.200	I	4.06	27.82 .07	25.80 .14	25.10 .04	24.41 .07	24.95 .09	1.63 .18	—	2.11 .03	27.86
1997 May 1.24	−5.39	0.200	H	4.21	27.81 .05	—	25.24 .01	24.45 .04	25.00 .04	2.36 .06	2.47 .02	2.49 .02	27.85
1997 May 1.24	−5.39	0.200	I	4.21	27.67 .09	25.75 .12	25.27 .02	24.44 .07	24.84 .10	1.87 .13	—	2.31 .02	27.71
1997 Jun 4.21	+28.58	0.206	I	4.73	27.71 .03	25.20 .14	25.20 .01	24.22 .12	24.91 .04	2.02 .11	—	2.30 .02	27.75
1997 Jun 4.23	+28.60	0.206	I	4.73	27.73 .03	25.37 .13	25.18 .02	24.59 .06	24.67 .13	1.52 .20	—	2.31 .02	27.76
1997 Jun 5.19	+29.56	0.207	I	4.73	27.78 .02	25.56 .10	25.24 .01	24.36 .08	24.99 .02	2.19 .08	—	2.28 .02	27.81
1997 Jul 1.21	+55.58	0.225	I	4.66	27.60 .05	25.43 .10	25.23 .01	24.43 .08	24.91 .05	1.85 .14	—	2.32 .02	27.62
1997 Jul 2.20	+56.57	0.225	H	4.66	27.76 .04	—	25.19 .01	24.41 .06	24.91 .03	2.26 .09	2.23 .04	2.36 .03	27.78
1997 Jul 2.20	+56.57	0.225	I	4.66	27.65 .05	25.37 .11	25.23 .01	24.29 .10	24.94 .04	2.13 .10	—	2.33 .02	27.67
1997 Jul 3.19	+57.56	0.226	H	4.66	27.70 .03	25.58 .04	25.15 .01	24.29 .06	24.95 .02	2.27 .08	2.24 .02	2.30 .02	27.72
1997 Jul 3.19	+57.56	0.226	I	4.66	27.50 .08	—	25.19 .02	—	24.87 .05	2.28 .13	—	2.35 .02	27.52
2003 Dec 22.55	+87.61	0.257	H	4.76	—	—	25.11 .09	—	24.79 .28	—	—	2.23 .26	—
2003 Dec 22.55	+87.61	0.257	H	4.55	—	—	24.82 .26	—	—	—	2.65 .24	2.64 .14	—
2003 Dec 22.56	+87.62	0.257	H	4.35	—	—	—	—	—	—	2.68 .26	—	—

[a]Filter set: A = A'Hearn and Millis; I = IHW; H = HB (see text and Appendix for details).

[b] Production rates, followed by uncertainties.

TABLE 4

Abundance Ratios for Comet 81P/Wild 2

Species	log Production Rate Ratios (X/OH)
OH	0.00
NH	–2.35±.34
CN	–2.60±.14
C_2	–2.97±.23
C_3	–3.40±.20
UV Cont.	–25.53±.32[a]
Blue Cont.	–25.40±.13[a]
Green Cont.	–25.28±.24[a]

[a] For the dust continuum, the ratio of $A(\theta)f\rho$ to Q(OH) has units of cm sec molecule^{-1}.

TABLE 5

Measured Position Angles and Widths of the Primary Jet in Comet 81P/Wild 2

UT Date (1997)	ΔT (day)	PA_{jet} (°)	$Width_{jet}$ (°)
Feb 1.5	–94.1	31±3	60
Feb 14.3	–81.3	31±3	45
Mar 1.2	–66.4	27±5	60
Mar 5.3	–62.4	22±3	60
Mar 16.4	–51.2	27±3	55
Mar 31.2	–36.4	33±4	60
Apr 25.2	–11.4	49±5	60

TABLE 6

Pole Solutions and Source Locations for Comet 81P/Wild 2

α (°)	δ (°)	λ (°)	β (°)	Orbital Longitude of the Pole[a] (°)	Obliquity of the Pole (°)
281±5	+13±7	283±5	+36±7	103±6	56±7

Constraint on Source Latitude (°)	
Primary	Secondary
> +75	–37 to –62

[a] The orbital longitude is the angle around the comet's orbital plane measured from the anti-solar direction at perihelion.

TABLE A1
IHW Coefficients for OH Extinction

			Comet[a]	
Coeff.	B Star	G Star	pure OH	25% cont.
Rayleigh				
b_1	1.177	1.163	1.171	1.169
b_2	-1.039×10^{-3}	-2.088×10^{-3}	—	-2.814×10^{-4}
b_3	-6.434×10^{-4}	-1.217×10^{-3}	—	-3.991×10^{-4}
Ozone				
c_{00}	—	2.794×10^{-1}	—	1.907×10^{-2}
c_{01}	—	-5.515	—	1.380
c_{02}	—	$4.050\times10^{+1}$	—	$-2.259\times10^{+1}$
c_{03}	—	$-1.149\times10^{+2}$	—	$1.022\times10^{+2}$
c_{04}	—	$1.014\times10^{+2}$	—	$-1.247\times10^{+2}$
c_{10}	-9.430×10^{-2}	-6.049×10^{-1}	3.380	8.054×10^{-2}
c_{11}	5.498	$1.577\times10^{+1}$	-1.456×10^{-2}	-1.380
c_{12}	-7.298	$-8.666\times10^{+1}$	—	$5.903\times10^{+1}$
c_{13}	9.044	$2.411\times10^{+2}$	—	$-2.411\times10^{+2}$
c_{14}	6.639×10^{-1}	$-2.080\times10^{+2}$	—	$2.794\times10^{+2}$
c_{20}	1.218×10^{-1}	4.533×10^{-1}	-5.866×10^{-3}	-1.778×10^{-1}
c_{21}	-1.941	-8.970	-5.431×10^{-2}	5.449
c_{22}	7.342	$6.260\times10^{+1}$	—	$-5.433\times10^{+1}$
c_{23}	-7.292	$-1.721\times10^{+2}$	—	$1.996\times10^{+2}$
c_{24}	-5.209	$1.435\times10^{+2}$	—	$-2.176\times10^{+2}$
c_{30}	-4.378×10^{-2}	-1.403×10^{-1}	—	9.373×10^{-2}
c_{31}	6.368×10^{-1}	2.711	—	-2.292
c_{32}	-2.496	$-1.919\times10^{+1}$	—	$1.980\times10^{+1}$
c_{33}	8.757×10^{-2}	$4.914\times10^{+1}$	—	$-6.708\times10^{+1}$
c_{34}	4.456	$-3.913\times10^{+1}$	—	$6.852\times10^{+1}$
c_{40}	4.360×10^{-3}	1.486×10^{-2}	—	-1.382×10^{-2}
c_{41}	-5.973×10^{-2}	-2.856×10^{-1}	—	3.011×10^{-1}
c_{42}	1.389×10^{-1}	1.916	—	-2.404
c_{43}	4.231×10^{-1}	-4.619	—	7.494
c_{44}	-8.370×10^{-1}	3.544	—	-7.214

[a] Comet coefficients represent the extreme cases of pure OH emission and 25% underlying continuum.

TABLE A2
AM Coefficients for OH Extinction

Coeff.	B Star	G Star	Comet[a] pure OH	Comet[a] 25% cont.
Rayleigh				
b_1	1.103	1.089	1.171	1.148
b_2	-8.104×10^{-3}	-9.461×10^{-3}	—	-1.743×10^{-3}
b_3	—	—	—	-3.737×10^{-4}
Ozone				
c_{00}	7.881×10^{-3}	-2.330×10^{-2}	3.350	-3.670×10^{-1}
c_{01}	1.331×10^{-1}	4.023×10^{-1}	-1.234×10^{-2}	6.710
c_{02}	9.755×10^{-1}	-5.843×10^{-2}	—	$-4.900\times10^{+1}$
c_{03}	-7.289×10^{-1}	3.303×10^{-1}	—	$1.832\times10^{+2}$
c_{04}	—	—	—	$-3.390\times10^{+2}$
c_{05}	—	—	—	$2.360\times10^{+2}$
c_{10}	8.286×10^{-3}	4.772×10^{-2}	-5.470×10^{-3}	6.388×10^{-1}
c_{11}	2.571	1.917	-5.531×10^{-2}	-8.520
c_{12}	-3.044	-1.342	—	$8.612\times10^{+1}$
c_{13}	1.691	5.753×10^{-2}	—	$-3.299\times10^{+2}$
c_{14}	—	—	—	$6.211\times10^{+2}$
c_{15}	—	—	—	$-4.341\times10^{+2}$
c_{20}	9.704×10^{-3}	-7.050×10^{-3}	—	-3.873×10^{-1}
c_{21}	-4.363×10^{-1}	-2.344×10^{-1}	—	7.067
c_{22}	2.970×10^{-1}	-2.844×10^{-1}	—	$-5.478\times10^{+1}$
c_{23}	-4.391×10^{-2}	5.364×10^{-1}	—	$2.132\times10^{+2}$
c_{24}	—	—	—	$-4.057\times10^{+2}$
c_{25}	—	—	—	$2.822\times10^{+2}$
c_{30}	-1.074×10^{-3}	7.850×10^{-4}	—	1.036×10^{-1}
c_{31}	2.569×10^{-2}	4.410×10^{-3}	—	-1.946
c_{32}	3.560×10^{-4}	6.307×10^{-2}	—	$1.512\times10^{+1}$
c_{33}	-1.863×10^{-2}	-8.205×10^{-2}	—	$-6.071\times10^{+1}$
c_{34}	—	—	—	$1.145\times10^{+2}$
c_{35}	—	—	—	$-7.814\times10^{+1}$
c_{40}	—	—	—	-1.030×10^{-2}
c_{41}	—	—	—	1.964×10^{-1}
c_{42}	—	—	—	-1.559
c_{43}	—	—	—	6.214
c_{44}	—	—	—	$-1.140\times10^{+1}$
c_{45}	—	—	—	7.577

[a] Comet coefficients represent the extreme cases of pure OH emission and 25% underlying continuum.

TABLE A3
IHW Filter Calibration Coefficients

Species[a]	F_{0XX}[b]	$m_{/XX}$	$\gamma_{XX/XX}$	$\gamma'_{XX/XX}$
OH	12.70	+2.257	1.18×10^{-2}	0.90
NH[c]	10.50	+1.596	1.19×10^{-2}	0.85
CN	10.4	+1.451	2.15×10^{-2}	0.99
C_3	9.673	+0.859	3.25×10^{-3}	0.24
CO^+	8.726	+0.743	1.41×10^{-2}	0.96
C_2	4.519	−0.048	5.93×10^{-3}	0.51
H_2O^+	1.612	−0.891	4.53×10^{-3}	0.99
UC	8.330	+1.174	—	—
BC	4.990	0.000	—	—
RC	1.732	−0.872	—	—

[a] Filter specification represented by XX subscript.

[b] Flux of 0 magnitude star (10^{-9} erg cm^{-2} sec^{-1} Å^{-1}).

[c] Original 1979 values; by 1997, progressive filter degradation resulted in $\gamma = 6.76\times10^{-3}$.

TABLE A4
IHW Contamination Coefficients

Gas

Species[a]	γ_{XX/C_3}
NH/C_3	2.15×10^{-5}
CN/C_3	1.47×10^{-3}
CO^+/C_3	4.73×10^{-4}

Continuum

Species[a]	K_{XX1}	K_{XX2}	K_{XX3}	K_{XX4}
BC/C_2	0.0559	0.0645	0.0494	0.0573
UC/C_3	0.1569	—	0.1246	—

[a] First species is represented by XX subscript; second species is the contaminant.

TABLE A5
AM Filter Calibration Coefficients

Species[a]	F_{0XX}[b]	$m_{\lambda XX}$	$\gamma_{XX/XX}$	$\gamma'_{XX/XX}$
OH	8.90	+2.085	4.92×10^{-3}	0.95
NH[c]	7.116	+1.581	1.19×10^{-2}	0.85
CN	7.56	+1.514	2.44×10^{-2}	0.93
C_3	7.252	+0.963	4.36×10^{-3}	0.09
C_2	3.575	+0.050	6.79×10^{-3}	0.48
UC	5.778	+1.105	—	—
GC	3.348	0.000	—	—

[a] Filter specification represented by XX subscript.
[b] Flux of 0 magnitude star (10^{-9} erg cm^{-2} sec^{-1} $Å^{-1}$).
[c] Original 1979 values; by 1997, progressive filter degradation resulted in $\gamma = 6.76\times10^{-3}$.

TABLE A6
AM Contamination Coefficients

Gas

Species[a]	γ_{XX/C_3}
NH/C_3	2.70×10^{-5}
CN/C_3	1.44×10^{-3}

Continuum

Species[a]	K_{XX1}	K_{XX2}	K_{XX3}
GC/C_2	0.0419	0.0374	0.0401
UC/C_3	0.1531	—	0.1093

[a] First species is represented by XX subscript; second species is the contaminant.

TABLE A7
KW Filter Calibration Coefficients

Species[a]	$F_{\lambda XX}/F_{\lambda BC}$	$\gamma_{XX/XX}$	$\gamma'_{XX/XX}$
CN	0.485	2.12×10^{-2}	1.00
C_3	0.835	3.43×10^{-3}	0.33
C_2	0.995	6.83×10^{-3}	0.65

[a] Filter specification represented by XX subscript.

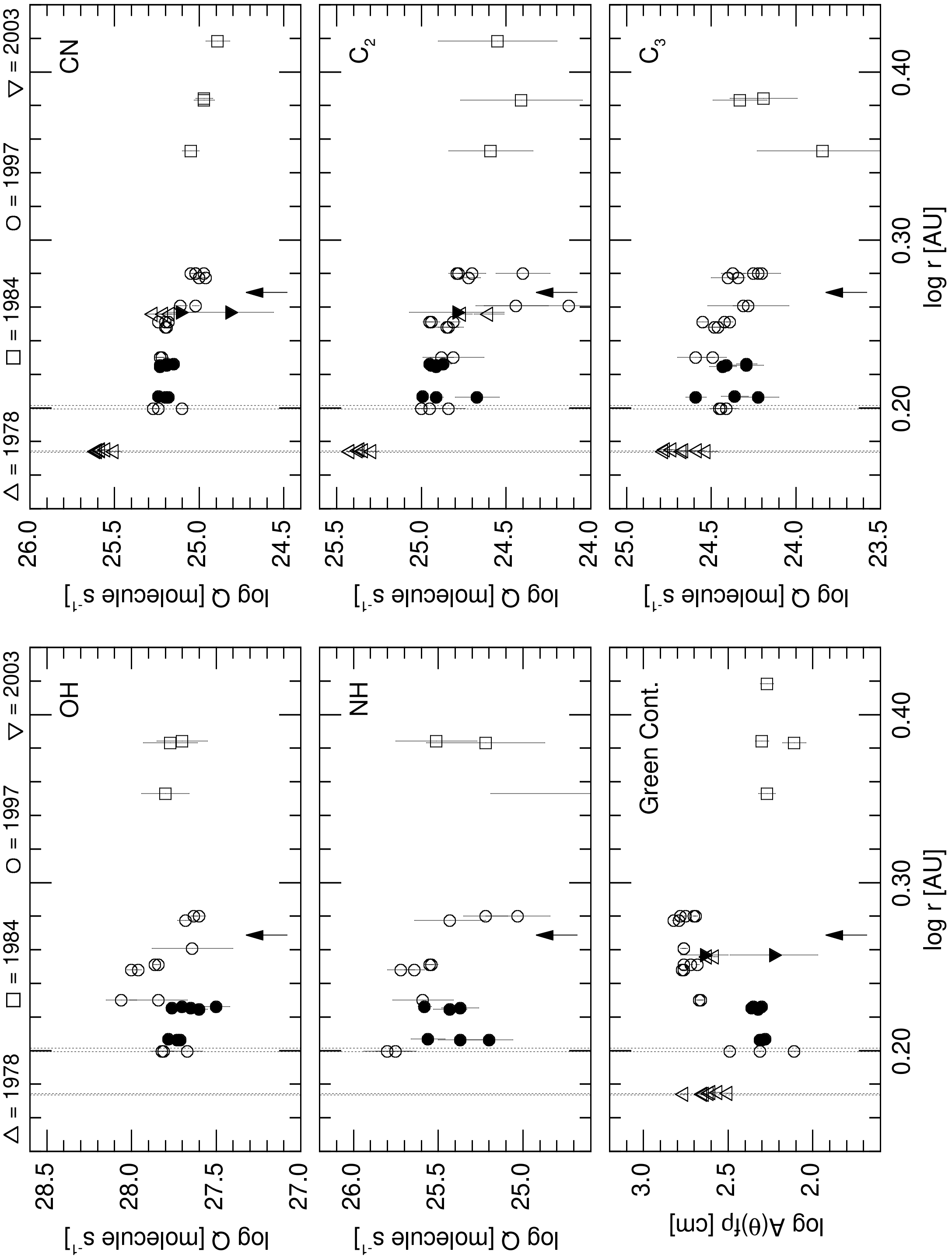

Fig. 1. Log of the production rates for each observed molecular species and $A(\theta)f\rho$ for the green continuum plotted as a function of the log of the heliocentric distance. Different symbols distinguish the four apparitions (see key at top); open symbols represent data obtained before perihelion while filled symbols are used for post-perihelion measurements. Vertical dotted lines represent perihelion distances, which have progressively increased for each apparition since 1978. Note the large asymmetries evident for both OH and NH, but not for CN nor C_2. The arrow indicates the post-perihelion distance corresponding to the Stardust encounter on 2004 January 2.

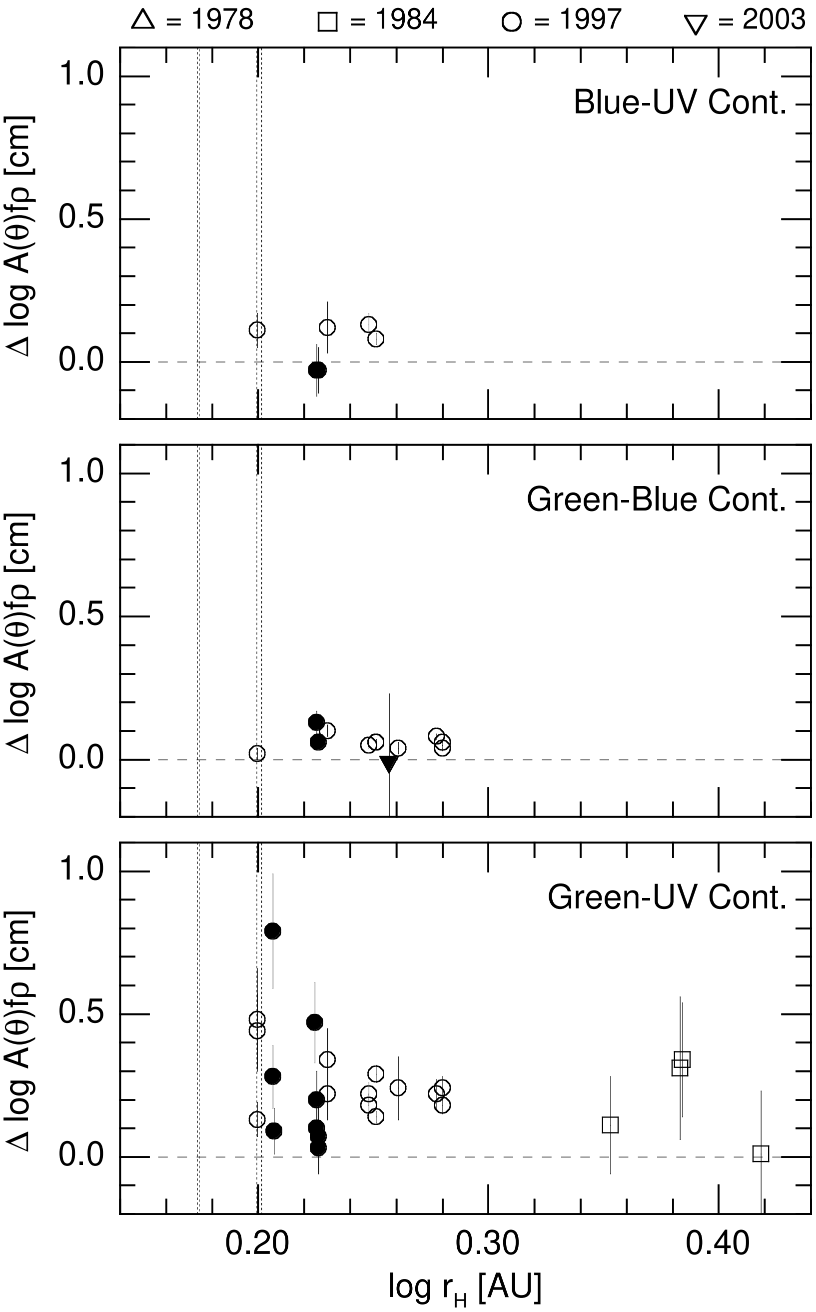

Fig. 2. Log of the dust colors as a function of the log of r_{H}. Symbols are the same as in Figure 1. The color of the dust is shown as the differential $A(\theta)f\rho$ for blue and UV continuum bandpasses (top), green and blue (middle), and green and UV (bottom). The dust colors show no evidence of trends with heliocentric distance nor with aperture size. Note that a portion of the scatter among data points in the bottom panel is due to changes in the spectral locations of the UV and green continuum bandpasses for the different filter sets. Note that no colors are available from the 1978 apparition due to the lack of a suitable UV continuum filter.

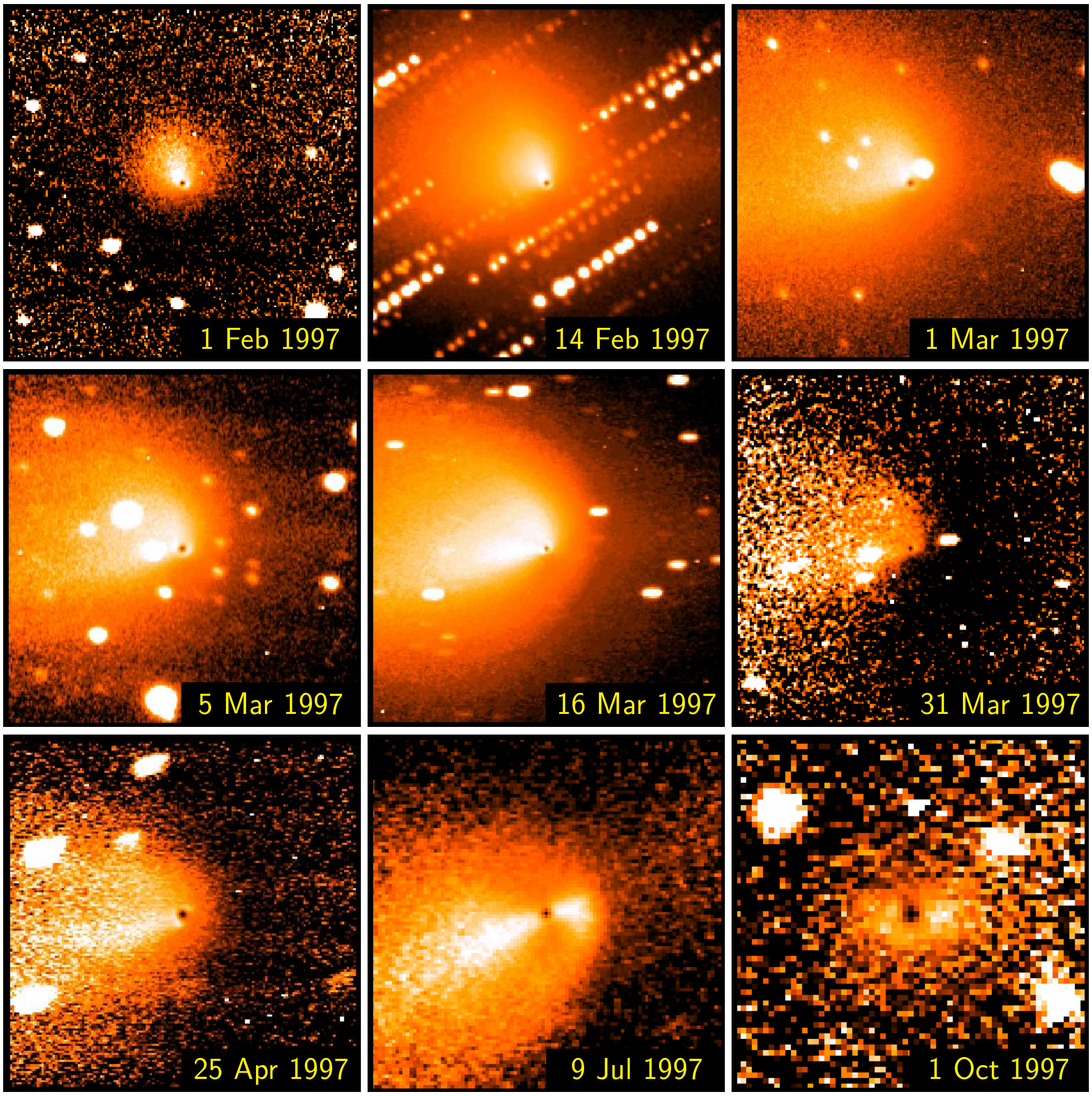

Fig. 3. Comet Wild 2 coma morphology as a function of time. For each CCD observing run, a representative dust image is shown, enhanced by removing a ρ^{-1} profile to reduce the bulk falloff of the coma. The optocenter is centered in each frame and is represented by the small dark spot (an artifact of the enhancement process). In all images, North is up, East is to the left, and the field of view corresponds to a distance of $1.4{\times}10^5$ km at the comet. Note the fan that consistently lies to the NNE from February through April, and the sharply defined jet to the West in July. The dust tail, which reflects the orientation of the orbital plane at a PA around 110°, is starting to form in early March and becomes more prominent through July. All images were obtained with a broadband R filter, except for those from 31 March and 25 April, which were obtained using the HB narrowband red continuum (RC) filter.

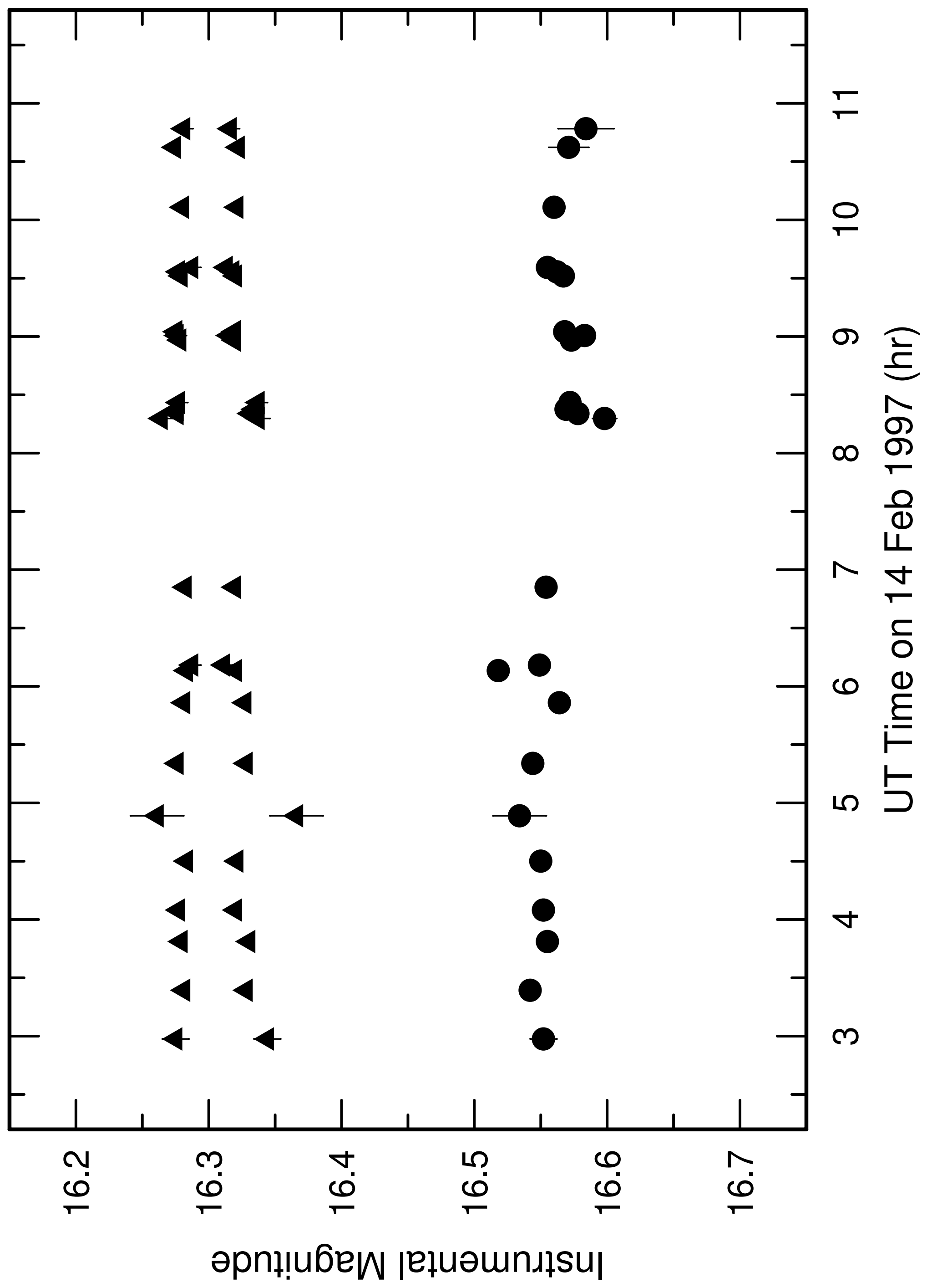

Fig. 4. Lightcurve for Comet Wild 2 on 14 February 1997, obtained with a broadband R filter over an eight hour time span. The circles represent the comet and the triangles represent comparison stars of similar brightness in the same field of view. During this time, there are no clear brightness variations at a level of 0.05 mag, and nothing to suggest any periodicity that could be used to constrain the rotation period of the nucleus.

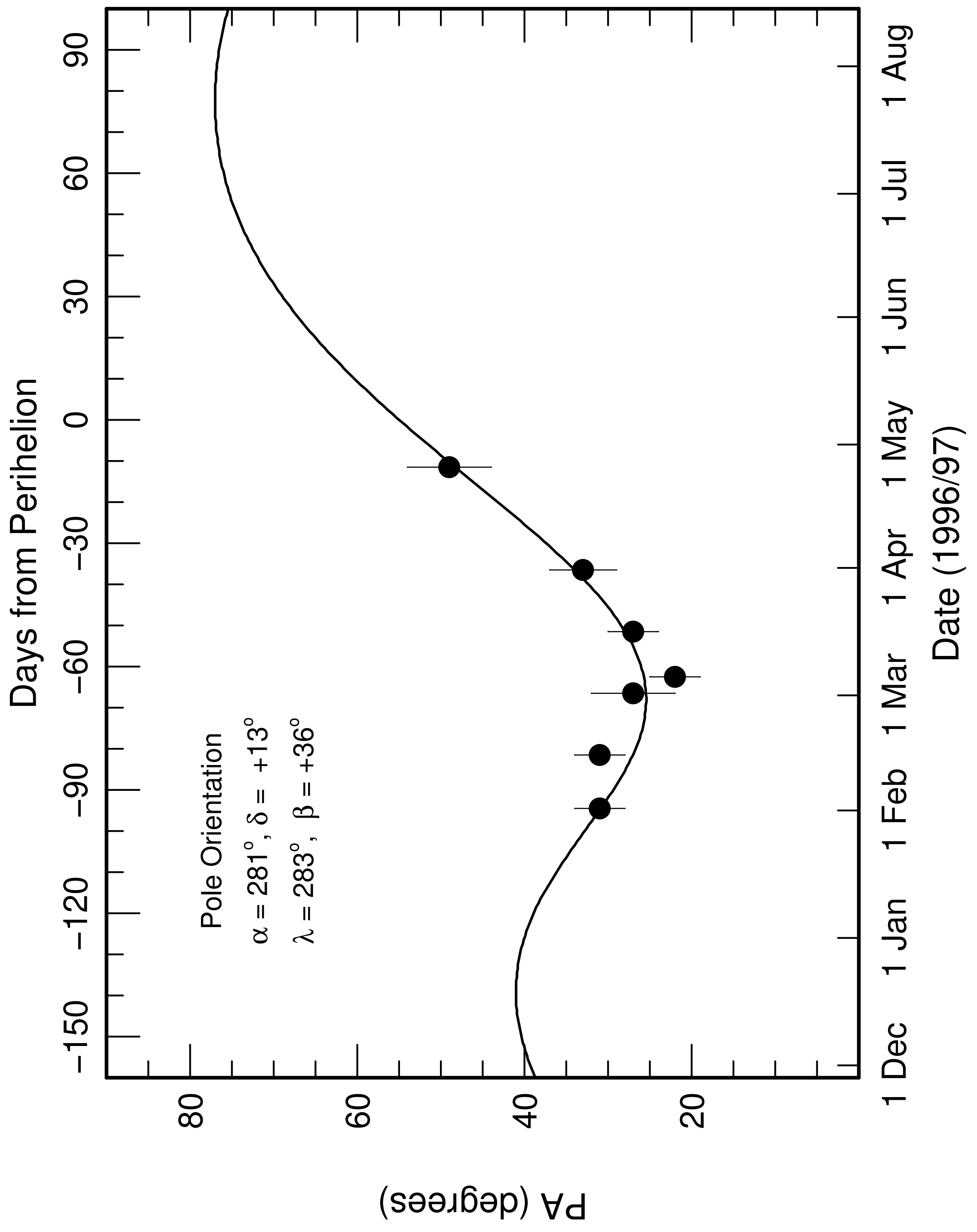

Fig. 5. The apparent position angle of the spin axis as a function of time. The circles denote measurements of the primary jet from our images, while the solid curve represents the computed PA for our best fitting pole solution.

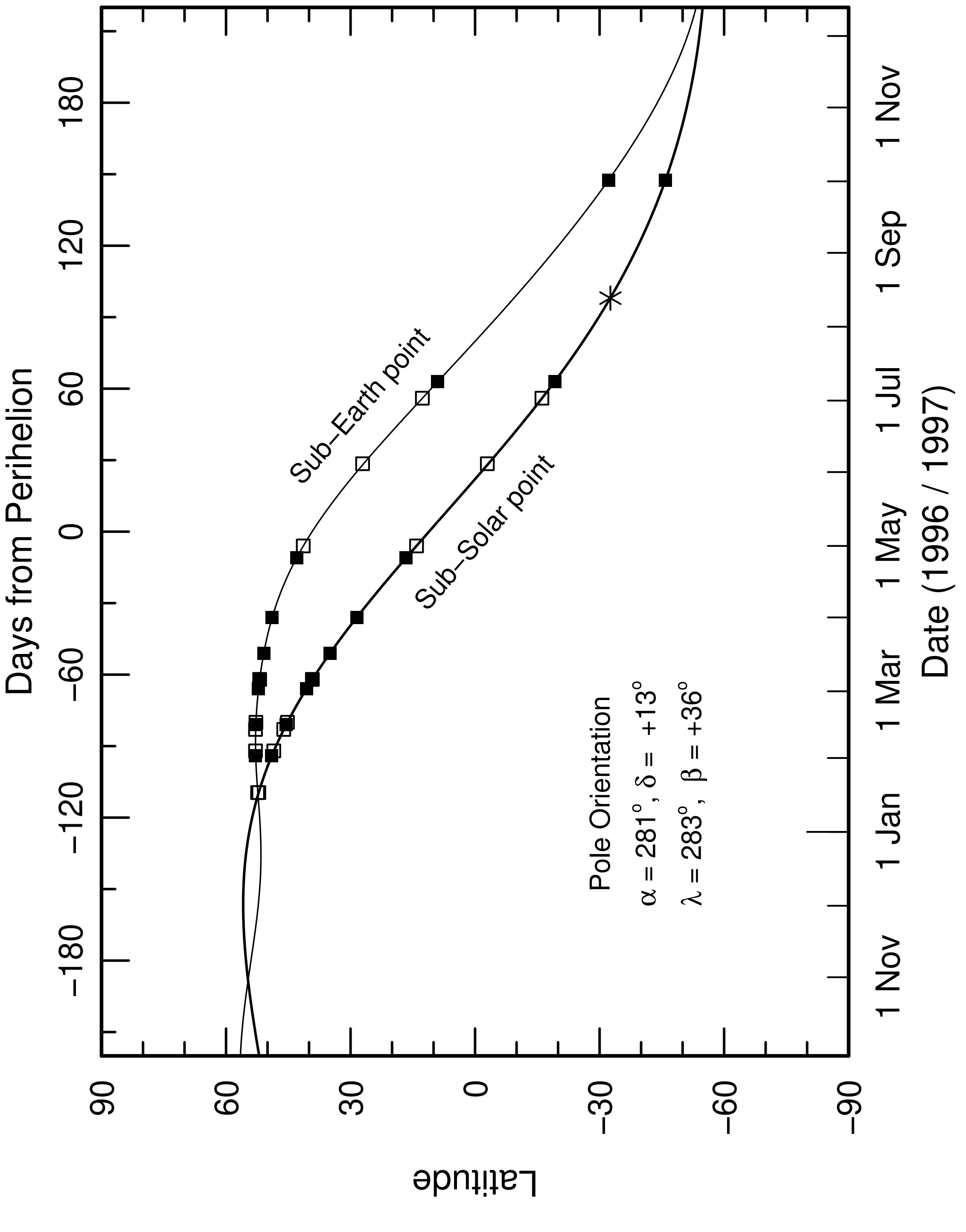

Fig. 6. The sub-solar and sub-Earth latitudes for comet Wild 2 as a function of time, given our derived pole orientation. The sub-solar latitudes are approximately representative of the 1984, 1991 and 2003 orbits, as well as for the 1997 apparition, but the sub-earth latitudes are specific to 1997. The northern hemisphere is defined as the one containing the primary jet. The squares denote the dates on which our 1997 observations were obtained, with solid squares representing CCD data and open squares representing photometry. The star denotes the corresponding time of the Stardust spacecraft encounter in 2004.

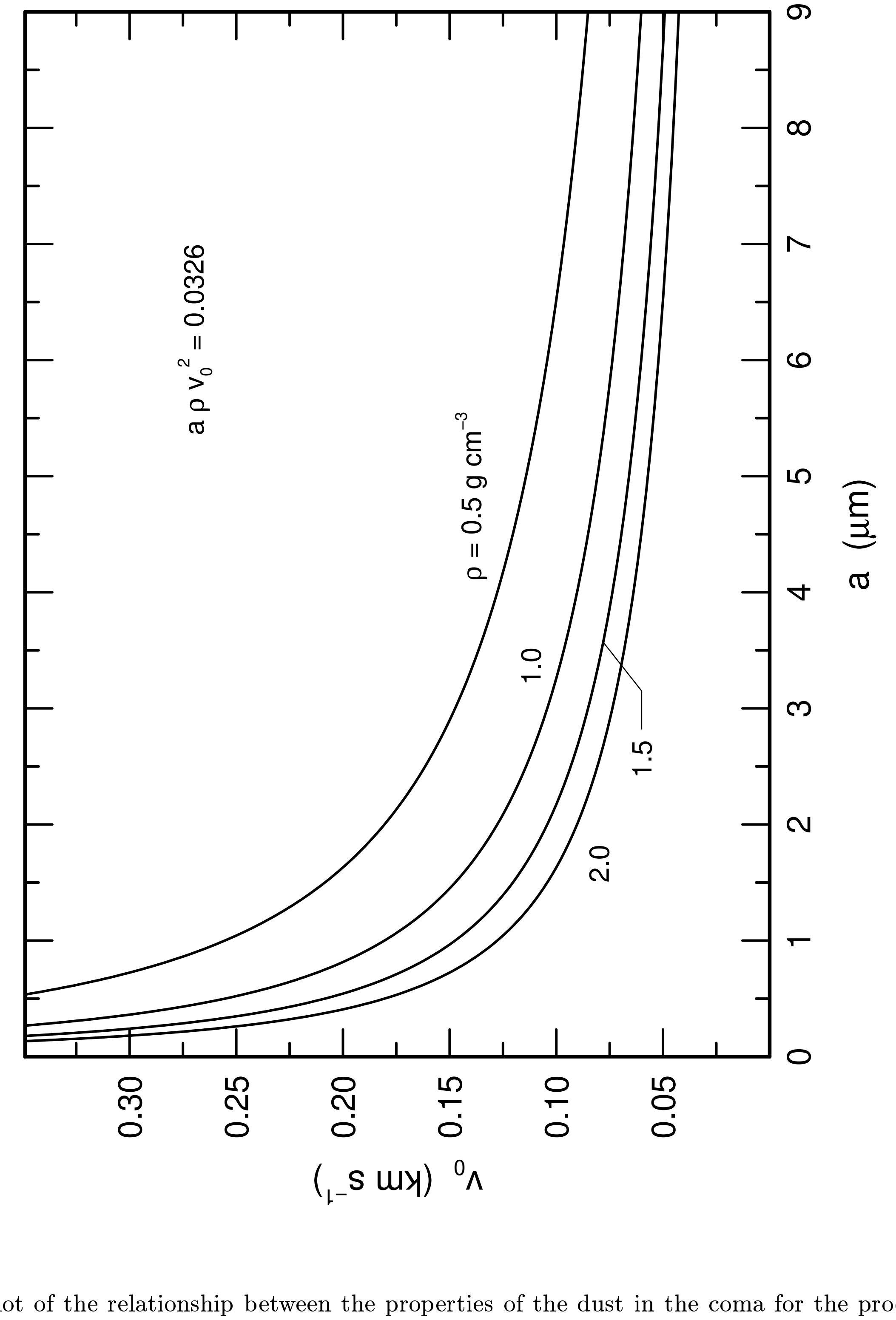

Fig. 7. Plot of the relationship between the properties of the dust in the coma for the product $a\rho v_o^2$=0.0326. This quantity is derived from the distance at which spherical dust grains of radius, a, density, ρ, and a terminal velocity, v_o, are turned around under the action of radiation pressure from the Sun.

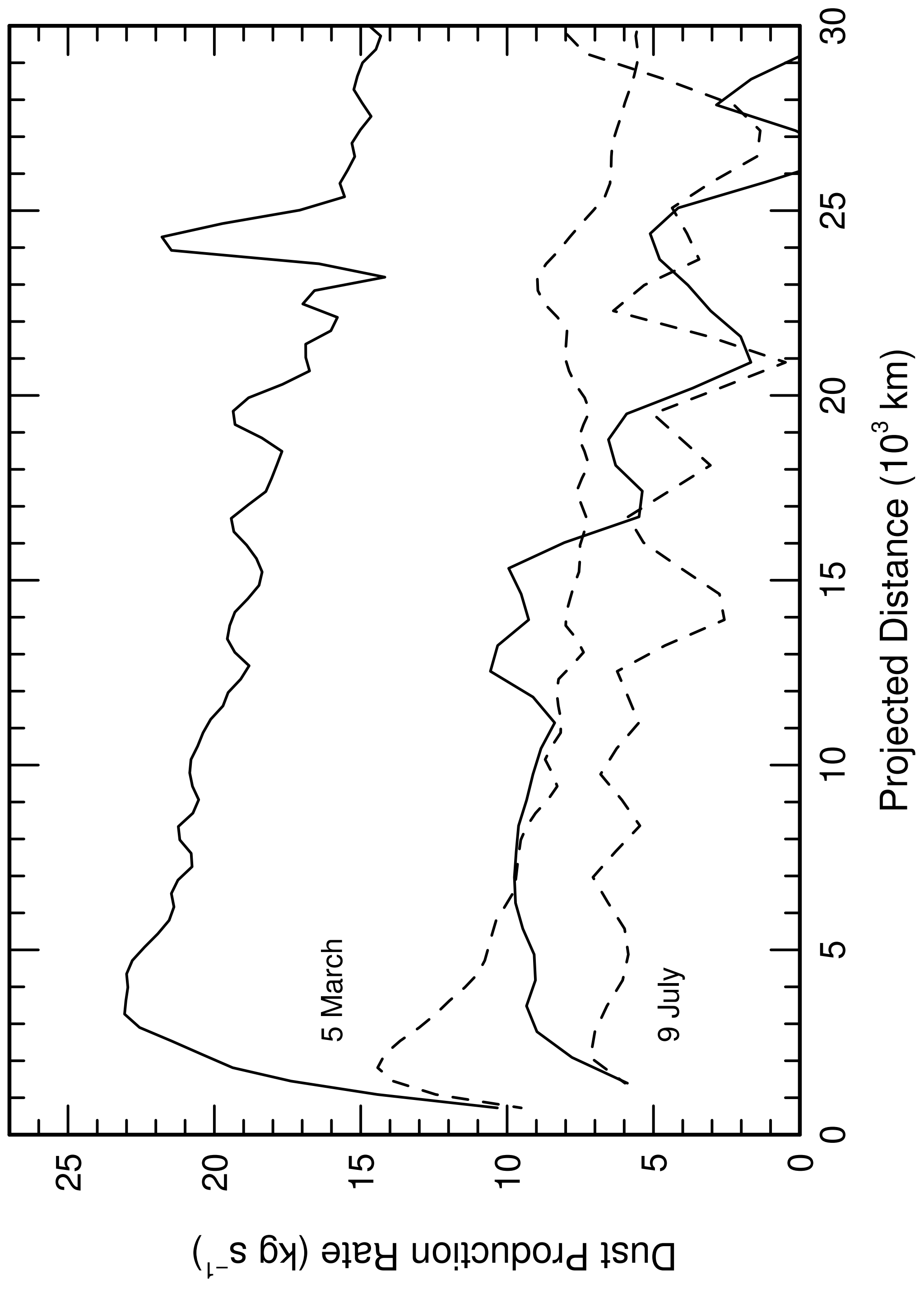

Fig. 8. Dust production rates, derived from the surface brightness profiles, as a function of distance from the nucleus. The solid curves represent the profiles along the jets (the primary on 5 March and the secondary on 9 July), and the dashed lines represent the profiles in the most quiescent direction, away from both the jet and the dust tail. The drop near the nucleus is an artifact produced by the removal of the ρ^{-1} profile in the conversion of surface brightness to dust production, and the large, sharp peaks correspond to regions where star trails cross the profile.

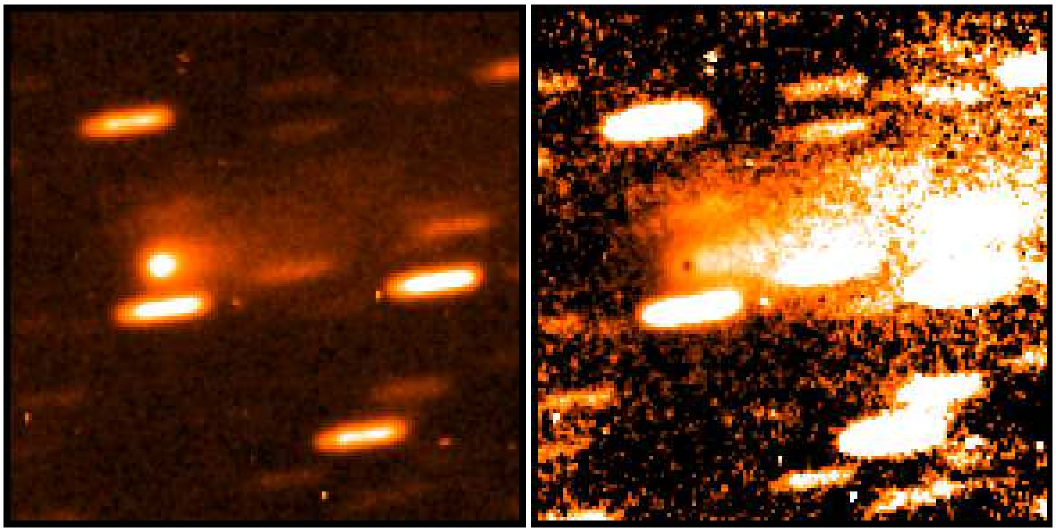

Fig. 9. Image of comet Wild 2 from 5 January 2004, just three days after the Stardust encounter. The left panel shows the original unprocessed image (the sum of six 120 s R exposures). The right panel is the same image enhanced by removing a ρ^{-1} profile to remove the bulk falloff of the coma. North is up, East is to the left, and the field of view corresponds to a distance of 3×10^5 km at the comet. Other than the dust tail extending to the west, there are no features visible.

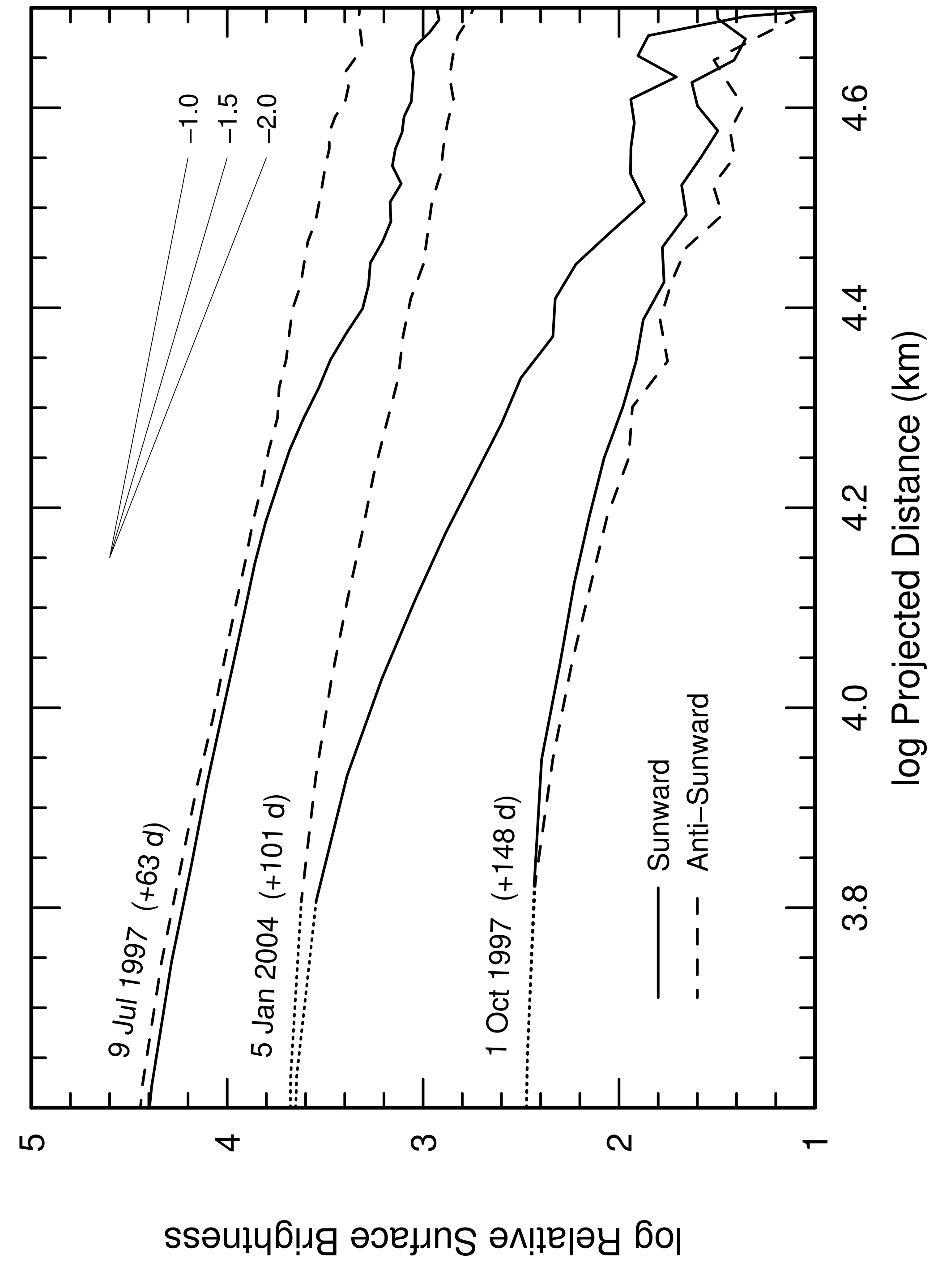

Fig. 10. Surface brightness profiles for the 2004 image in the sunward and anti-sunward directions. For comparison, the two profiles from 1997 that bracket the corresponding observation time are also shown. Note the extreme slope of the 2004 coma in the sunward direction — comparable to the drop in the July 1997 curve between log(distance) of 4.2 and 4.4, which corresponds to the edge of the parabolic envelope. The three pairs of curves are offset vertically for clarity, and the dotted portions of the October 1997 and January 2004 curves denote the region inside the seeing disk, which causes that portion of the profile to flatten out.